Contents

Chapter 1

Introduction

The European Laboratory for Particle Physics (CERN) is the world's leading research center in experimental particle physics. CERN was founded in 1954 and it currently has 20 member states, including Finland from the year 1991 onwards. The laboratory is situated astride the Franco-Swiss border, west of Geneva at the foot of the Jura mountains.

The latest large accelerator at CERN was the Large Electron Positron collider (LEP) which ended operation in 2000. It produced high-precision data for testing the Standard Model, the best description of the subatomic world available today. The LEP measurements were so accurate that they provided insight into what may happen at energies beyond those of the machine itself. All evidence indicates that new physics, and answers to some of the most profound questions of our time, lie at collider energies above 1 TeV. This is why a new accelerator, the Large Hadron Collider (LHC) is to be built at CERN. It will reach higher energies than any previous accelerator, and notably exceed the present record energy of the Tevatron at Fermilab with 1 TeV p and $\bar{p}$.

The LHC is being built inside the 27-kilometer long circular LEP tunnel. It has been primarily designed to collide protons at an energy of 7 TeV each, adding up to 14 TeV center of mass energy. The LHC will be fed by existing particle sources and pre-accelerators. In the collider itself, protons travel clockwise and anticlockwise in two different beam pipes. At four interaction points the protons are made to collide head on.

One of the main goals of the LHC is to explain the origin of the mass of elementary particles, which is one of the fundamental questions in particle physics. The standard model comes up with an explanation called the Higgs mechanism. The particle masses are created by an interaction with a hypothetical Higgs field. The model predicts a new scalar particle, the Higgs boson, that will mediate the interaction. It has not yet been discovered but if such a particle exists, the LHC should be able to detect it.

The conventional way to detect the Higgs boson is to measure the en-

ergy and the angle of its decay particles after the Higgs boson has been produceed in hard scattering. The general purpose detectors ATLAS and CMS are optimised to detect isolated high-energy photons and leptons that are produced in some decay channels. However, the signal is accompanied with a huge background. One alternative, and a less studied way to detect the Higgs boson, is to measure the scattered protons in exclusive processes. The number of Higgs events in exclusive processes is predicted to be rather small but the signal-to-background ratio is attractive.

The aim of this thesis is to examine the experimental aspects of the measurement of the leading protons, i.e. the outgoing protons from such an exclusive process. A method was developed to reconstruct the kinematics of the scattered protons from observed trajectories at several carefully selected locations. With this reconstruction method, the resolution and possible systematic biases on the momentum loss measurement were studied and applied to the mass resolution of the hypothetical Higgs boson.

Chapter 2

Theory

2.1 Standard Model

The Standard Model (SM) is an attempt to describe the basic phenomena in particle physics. Within the SM, there are three types of particles: quarks, leptons and gauge bosons. Quarks and leptons, both fermions as they obey Fermi statistics, are the fundamental constituents of matter. They are spin-1/2 particles and they form three families, each containing a left-handed quark and lepton doublet and a right-handed quark and lepton singlet.

Table 2.1: Standard Model particles and their interactions.

Fermions	Quarks	u	s	b
		d	c	t
	Leptons	e	μ	τ
		ν_e	ν_μ	ν_τ
Bosons	Electromagnetic	γ		
	Weak interaction	W^+, W^-, Z^0		
	Strong interaction	gluons (8)		

There are four fundamental interactions between fermions: the electromagnetic, strong, weak and gravitational interaction. Only the gravitational interaction has not been incorporated into the Standard Model. The strength of the gravitational interaction between the elementary particles is so weak that it has no observable effects at the energies used in experimental particle physics. These fundamental interactions are mediated by the exchange of gauge bosons, which carry unit spin [1].

The gauge bosons of the electromagnetic and strong interactions, photons and gluons, are massless particles. The weak interaction is mediated

3

by the massive vector bosons, $W^\pm$ and Z^0. In local gauge invariant theories, where the observed physical quantities do not depend on a particular choice of the potential used to describe the fields, gauge bosons should be massless. In the Standard Model this is solved, still preserving the gauge invariance, by introducing spontaneous symmetry breaking.

This symmetry breaking is called the Higgs mechanism. In the Higgs mechanism, the scalar Higgs field creates masses to the massive vector bosons $(W^\pm, Z^0)$, and one massive scalar boson (H). This scalar boson is called Higgs boson and its mass is a free parameter of the Standard Model. The fermion masses can be explained by Yukawa coupling of the Higgs boson to the fermions.

The Higgs boson has not yet been found experimentally and there is a huge effort to find evidence for it. The results from the LEP accelerator restrict the Higgs mass to value of M_H>114 GeV. In the Standard Model description of the electroweak data, the virtual effects favour a Higgs mass to be just above the LEP bound [2].

In particle physics, it is a common choice to use the natural units with $\hbar=c=1$. In the natural units, the units of mass and momentum reduce to those of energy. It is customary to measure quantities in units of GeV, a choice motivated by the fact that the rest energy of the proton is roughly 1 GeV.

2.1.1   Quantum Electrodynamics

Elementary particle interactions can be described with Feynman diagrams, as depicted in Fig. 2.2. The contribution of each diagram to the propability amplitude for a given physical process can be calculated by a set of mathematical rules. For electromagnetic interactions, this theory is called Quantum Electrodynamics (QED) and the resulting theoretical predictions have been verified experimentally.

The symmetries of the theory are described by a $U(1)$ group. QED is the simplest example of a gauge theory in the sense that it has only one gauge particle, photon.

The strength of electromagnetic interactions between two charged particles is expressed by the electromagnetic coupling constant

$$\alpha(Q^2) = \frac{\alpha(\mu^2)}{1 - \frac{\alpha(\mu^2)}{3\pi} \log\left(\frac{Q^2}{\mu^2}\right)}. \tag{2.1}$$

In this formula, Q^2 is the energy range and μ^2 is defined as the value of Q^2 in case of physical (renormalized) charges. At low energies $\alpha \simeq 1/137$.

2.1.2   Quantum Chromodynamics

The part of the Standard Model describing strong interactions is called Quantum Chromodynamics (QCD). It introduces a hidden quantum number, colour, associated with the strongly interacting particles, quarks and gluons. Each quark carries a colour charge, which can be exchanged by the bicoloured gluons. The different colours have been chosen to be named as red, green and blue. Each colour has also its anticolour. In all physical particles composed of quarks, the quarks are combined in such a way as to result in a colourless overall particle. The bound states of quark-antiquark pairs are referred to as mesons and the three quark states with equal mixtures of all colours or anticolours are called baryons [3].

The symmetries of the theory are described by a $SU(3)$-group, which implies that there are altogether eight different gluon colour combinations, and the gluons also couple to each other in addition to the ordinary colour charges.

The strength of strong interactions between two coloured particles is expressed through the strong coupling constant α_s. Its behaviour as a function of an energy scale can be formulated as

$$\alpha_s(Q^2) = \frac{\alpha_s(\mu^2)}{1 + \frac{\alpha_s(\mu^2)}{12\pi}(33 - 2N_F)\log(Q^2/\mu^2)}, \qquad (2.2)$$

where N_F is the number of quark flavours at the given energy range Q^2 and μ^2 is defined as the value of Q^2 in case of physical (renormalized) colour charges. According to Eq. (2.2), as Q^2 increases, the value of α_s decreases. Thus the coupling becomes small for interactions at high energies, which according to the uncertainty principle is equivalent to interactions at small distances. This effect is called the asymptotic freedom of coloured particles.

By introducing a free parameter Λ through

$$\Lambda^2 = \mu^2 \exp\left[\frac{-12\pi}{(33 - 2N_F)\alpha_s(\mu^2)}\right], \qquad (2.3)$$

the expression for α_s can be written as

$$\alpha_s(Q^2) = \frac{12\pi}{(33 - 2N_F)\log(Q^2/\Lambda^2)}. \qquad (2.4)$$

When Q^2 is much larger than Λ^2, the effective coupling between colour charges is small, and the particles are in a quasi-free state with respect to strong interactions. However, when Q^2 is small, the quarks and gluons are combined into strongly bound colourless clusters, hadrons. The exact value of Λ is a free parameter not predicted by the theory, while experiments indicate that the numerical value is somewhere between 0.1 and 0.5 GeV.

    The Lagrangian density of QCD, the basis of all theoretical calculations, is given by

$$\mathcal{L} = \bar{q} \left(i\gamma^\mu \partial_\mu \right) q - g \left(\bar{q}\gamma^\mu T_a q \right) F_\mu^a - \frac{1}{4} F_{\mu\nu}^a F_a^{\mu\nu}. \qquad (2.5)$$

The q and $\bar{q}$ denote the quark and antiquark fields, respectively, and T_a with $a=1,...,8$ are a set of linearly independent traceless 3x3 matrices and γ^μ are the Dirac gamma matrices. The gauge fields $F_{\mu\nu}^a$ are defined as

$$F_{\mu\nu}^A = \partial_\mu \mathcal{A}_\nu^A - \partial_\nu \mathcal{A}_\mu^A - g f_{ABC} \mathcal{A}_\mu^B \mathcal{A}_\nu^C, \qquad (2.6)$$

$\mathcal{A}_\alpha^A$ is the spin-1 gluon field. The capital indices A, B, C run over eight colour degrees of freedom of the gluon field, and g is related to the QCD coupling constant α_s by $\alpha_s = g^2/4\pi$. The numbers f^{ABC} are the structure constants of $SU(3)$.

    For sufficiently small α_s it is possible to use perturbation theory in the calculations. Perturbation theory is not applicable, for example, to the bound-state problem of QCD with $\alpha_s \sim 1$. For large α_s practical calculations directly from the Lagrangian density of QCD are impossible.

2.2   Supersymmetry

Particle physics aims at unifying all the fundamental interactions. The electromagnetic and weak interactions have already been succesfully unified into the electroweak theory. The next goal is a grand unified theory (GUT), where the strong interaction would be combined with the electroweak theory. The most popular theories for grand unification include a new postulated symmetry of nature, supersymmetry. In supersymmetric models, all elementary particles have a supersymmetric partner, called a sparticle.

    In the minimal supersymmetric extension of the Standard Model (MSSM), the Higgs sector consists of two Higgs doublets which generate five physical Higgs states: h^0, H^0, A^0 and $H^\pm$. In the MSSM, there are two free Higgs parameters. A common choice is the mass of the A^0 and $\tan(\beta)$, which is the ratio of the vacuum expectation values of the two Higgs fields. The other Higgs masses depend on these two. In non-minimal models all the masses of the other sparticles have no predetermined values, and the models have more than 120 free parameters. No sparticle has yet been found experimentally, and the results from the LEP collider restrict the mass of the lightest supersymmetric particle $\tilde{\chi}_1^0$ to be $M_{\tilde{\chi}_1^0} > 37$ GeV [2].

2.3   Kinematics

The experimental signature of diffraction, see Section 2.4, consists of particular kinematical and topological configurations of the final state. In this

Section, the most common concepts of the kinematics of the scattering processes are defined and explained.

The center of mass energy is $E_{cms} = \sqrt{s}$, where s is one of the Mandelstam variables. For two-body interactions, the Mandelstam variables are defined as

$$\begin{aligned}
s &= (p_1 + p_2)^2 = (p_3 + p_4)^2 \\
&= m_1^2 + 2E_1 E_2 - 2\mathbf{p_1} \cdot \mathbf{p_2} + m_2^2,
\end{aligned} \tag{2.7}$$

$$\begin{aligned}
t &= (p_1 - p_3)^2 = (p_2 - p_4)^2 \\
&= m_1^2 - 2E_1 E_3 + 2\mathbf{p_1} \cdot \mathbf{p_3} + m_3^2,
\end{aligned} \tag{2.8}$$

$$\begin{aligned}
u &= (p_1 - p_4)^2 = (p_2 + p_3)^2 \\
&= m_1^2 - 2E_1 E_4 + 2\mathbf{p_1} \cdot \mathbf{p_4} + m_4^2,
\end{aligned} \tag{2.9}$$

where p_1 and p_2 are the 4-vectors of the incoming protons and p_3 and p_4 the 4-vectors of the outgoing protons. The Mandelstam variables satisfy

$$s + t + u = m_1^2 + m_2^2 + m_3^2 + m_4^2. \tag{2.10}$$

Frequently used dimensionless kinematic variables are rapidity and pseudorapidity. The rapidity y is defined as

$$y = \frac{1}{2} \ln \left(\frac{E + p_z}{E - p_z} \right) = \tanh^{-1} \left(\frac{p_z}{E} \right). \tag{2.11}$$

Under a boost in the z-direction to a frame with velocity $v/c = \beta$, the rapidity changes to $y \to y - \tanh^{-1} \beta$, and hence the form of the rapidity distribution is invariant under such boosts. This makes rapidity a very useful quantity in particle physics. For $p \gg m$, the expression for rapidity may be expanded to obtain

$$y = \frac{1}{2} \ln \frac{\cos^2(\theta/2) + m^2/4p^2 + ...}{\sin^2(\theta/2) + m^2/4p^2 + ...} \simeq -\ln \tan(\theta/2) \equiv \eta, \tag{2.12}$$

where $\cos(\theta) = p_z/p$. Here η is called pseudorapidity. The strong inequality $p \gg m$ holds for protons in high-energy accelerators, such as the LHC.

2.4   Diffractive scattering

Pertubative QCD theory allows a good description of hadronic interactions in hard processes ($\alpha_s \ll 1$). However, the total cross section is only partly covered by the hard processes. The rest is due to soft processes with $\alpha_s \sim 1$. They cannot be described within perturbative QCD, and other phenomenological theories are used for calculations of soft processes. Soft processes, in which no quantum numbers are exchanged between the colliding particles in a high-energy collision, are called diffractive processes.

2.4.1   Classification

The wave nature of particles leads to two classes of diffractive phenomena in hadron-hadron collisions: elastic scattering, i.e. $pp \rightarrow pp$, and diffractive dissociation. The elastic scattering is analogous to the classical diffraction of light. In the collision, both colliding particles remain intact and no new particles are created, i.e. the particles just exchange momenta. It can be described as scattering by a disc, for which the differential cross section has the form $d\sigma/dt \sim e^{bt}$, where $t = (p'-p)^2 \approx -p_T^2$ is the 4-momentum transfer and b is the slope parameter. The latter is related to the disc radius, R, via $b = R^2/4$.

In contrast to elastic scattering, the phenomenon of diffractive dissociation has no classical analogue. It may be thought of as a quasi-elastic scattering of two hadrons, where one of the hadrons is simultaneously excited into a higher mass state retaining its quantum numbers. This coherent excitation requires not only small transverse but also small longitudinal momentum transfer. For quasi-elastically scattered protons, the coherence condition for diffraction takes the form

$$\xi = \frac{M^2}{s} \leq \frac{m_\pi}{m_p} \approx 0.15, \qquad (2.13)$$

where M is the mass of the diffractive cluster, and ξ is the fraction of the momentum lost by the proton in the collision,

$$\xi = 1 - \frac{p_z}{p_{z,max}}. \qquad (2.14)$$

Diffractive dissociation can be further subdivided in three different classes: single diffraction, double diffraction and double Pomeron exchange (or central diffraction).

In single diffractive scattering ($pp \rightarrow p + X$), one of the two colliding protons stays intact, while the other dissociates into a final state X. The process has a very pronounced signature: a leading proton on one side, a few particles on the other side and between a gap in rapidity, where no particles are produced. Single diffraction accounts for approximately 10% of the total hadronic cross sections [6].

In double diffraction ($pp \rightarrow X_1 + X_2$), each incident particle gives rise to a set of final particles with exactly the same quantum numbers as for the two initial particles. Double diffractive events are characterized by a rapidity gap between the two systems.

The double Pomeron exchange process involves two Pomerons emitted from the initial protons. The two Pomerons collide, creating a diffractive system with activity in the central region. The signature implies two leading protons on both sides of the detector, activity in the central part and two rapidity gaps on both sides. Event topologies for diffractive dissociation
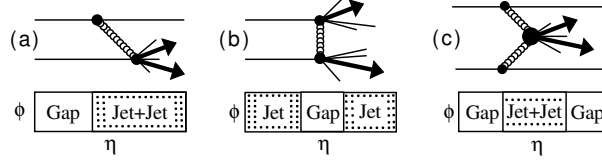
Figure 2.1: Dijet production diagrams and event topologies with jet production for (a) single, (b) double and (c) central diffraction.

are shown in Fig. 2.1, where the dissociative system(s) contain in addition jet(s).

All three processes can be tagged by the rapidity gap signature. Single diffraction and double Pomeron exchange can also be tagged by detecting the leading proton(s) on the gap side.

The total cross section at LHC energies is typically in the region of 100-120 mb. About 30% of this total cross section corresponds to elastic scattering, 10% to single diffraction, 3.5% to double diffraction and 1% to central diffraction. The rest of the total cross section is covered by minimum-bias events, which are inelastic events that do not fall into any of the categories above.

2.4.2   Regge theory

Hadron-hadron interactions, such as pp collisions, are described by QCD. However, calculating phenomena occuring in the proton collisions directly from the Lagrangian of QCD is a formidable challenge. Consequently, older phenomenological theories are used to describe diffractive scattering. Regge theory is one of them.

In the Regge theory approach hadronic interactions are described in terms of exchanges of Regge trajectories [7]. According to this theory, hadrons lie on Regge trajectories $l = \alpha(m^2)$ such that if m_i is the mass of meson i, and S_i is its spin, then $S_i = \alpha(m_i^2)$ with $S_i = 0, 1, 2, ...$ In the calculations, all possible trajectories should be taken into account.

For simplicity, let us consider particles lying on a single linear trajectory

$$\alpha(t) = \alpha_0 + \alpha' t \qquad (2.15)$$

such that $\alpha(t)$ passes through integer values of l at $t = m_l^2 (l = 0, 1, 2, ...)$. In this special case the propagator pole representing the scattering amplitude takes the form

$$A_l(t) \simeq \frac{\beta(t)}{l - \alpha(t)} \simeq \frac{\beta(t)}{\alpha'(m_l^2 - t)} \qquad (2.16)$$

i.e. there is a 'Regge pole' in the partial wave amplitude at $l = \alpha(t)$, and $\beta(t)$ is the residue function specifying the coupling of the pole to the external particles. The contribution of the trajectory to the amplitude is

$$A(s,t) \simeq \sum_{l=0}^{\infty} (2l + 1) \frac{\beta(t)}{1 - \alpha(t)} P_l(\cos\theta_t). \tag{2.17}$$

Owing to the asymptotic form $P_l(\cos\theta) \to (\cos\theta)^l$ as $\cos\theta \to \infty$ the amplitude simplifies into

$$A(s,t) \sim \sum_{l=0}^{\infty} \frac{\beta(t)(\cos\theta_t)^l}{l - \alpha(t)} \sim \beta(t)(\cos\theta_t)^{\alpha(t)} \sim \beta(t)\left(\frac{s}{s_0}\right)^{\alpha(t)}. \tag{2.18}$$

In the last step, the interchange rule $\cos\theta_t \sim s/s_0$ has been applied.

Equation (2.18) is the characteristic Regge-pole asymptotic power behaviour of the scattering amplitude as a function of s at fixed t stemming from the exchange of a Regge trajectory of composite particles. It predicts that in a two-body process the differential cross section as a function of momentum transfer is given by

$$\frac{d\sigma}{dt} \sim \frac{1}{s^2} |A(s,t)|^2 \sim F(t) \left(\frac{s}{s_0}\right)^{2\alpha(t)-2} \tag{2.19}$$

where $\alpha(t)$ is the leading Regge trajectory which can be exchanged.

The total, elastic and single diffractive cross sections due to the exchange of Regge trajectory are given by [5]

$$\sigma_T(s) = \beta_{R_{pp}}^2(0) \left(\frac{s}{s_0}\right)^{\alpha_R(0)-1} \tag{2.20}$$

$$\frac{d\sigma_{el}}{dt} = \frac{\beta_{R_{pp}}^4(t)}{16\pi} \left(\frac{s}{s_0}\right)^{2[\alpha_R(0)-1]} \tag{2.21}$$

$$\frac{d^2\sigma_{sd}}{d\xi dt} = \underbrace{\frac{\beta_{R_{pp}}^2(t)}{16\pi} \xi^{1-2\alpha_R(t)}}_{f_{R/p}(\xi,t)} \left[\beta_{R_{pp}}(0)g(t) \left(\frac{s'}{s_0}\right)^{\alpha_R(0)-1} \right] \tag{2.22}$$

where $\alpha_R = \alpha_R(0) + \alpha't = (1 + \epsilon) + \alpha't$ is the leading Regge trajectory, $\beta_{R_{pp}}(t)$ the coupling of the trajectory to the proton, $g(t)$ the RRR coupling, $s' = M^2$ the $R - p$ center-of-mass energy squared and s_0 an energy scale that is traditionally set to the hadron mass scale of 1 GeV^2.

The trajectory parameter $\alpha(0)$ is approximately 0.5 for a Reggeon trajectory. Inserting it into Eq. (2.20), one can see that total cross section
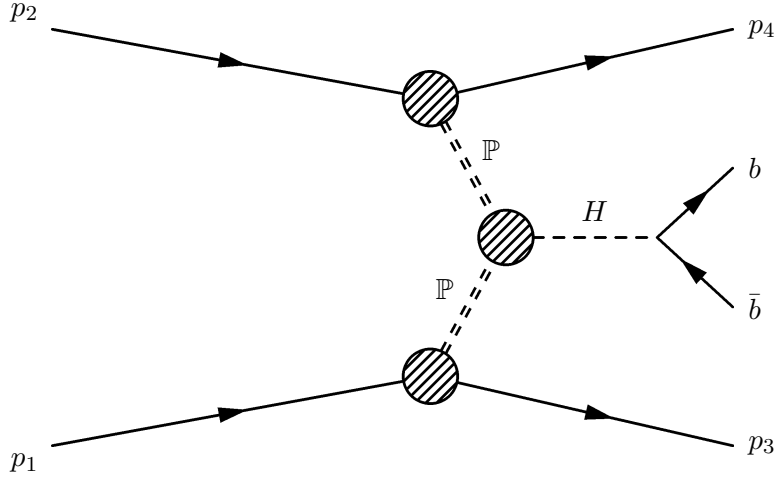
Figure 2.2: Feynman diagram describing exclusive double Pomeron ($\mathbb{P}$) exchange.

decreases as a function of center of mass energy. However, at energies above 10-20 GeV the total cross section starts to increase as a function of center of mass energy. This is due to exchange of the Pomeron trajectory, which dominates at high energies. The Pomeron $\mathbb{P}$ describes a colour singlet gluon exchange and its $\alpha(0) \simeq 1.1$.

Regge theory has been shown to provide a quantitatively reliable description of experimental data [9]. However, at higher energies the Regge approach becomes infested with unitarity problems. Nevertheless, the theory can still be used for phenomenological calculations.

2.4.3 Exclusive production of the Higgs boson

The Higgs boson can be produced in the exclusive double Pomeron exchange reaction. In the exclusive process $pp \rightarrow p + H + p$ with $H \rightarrow b\bar{b}$, where the $+$ sign indicates the presence of a rapidity gap, it is possible to tag the outgoing protons in such a way that the Higgs boson can be identified. By requiring the presence of rapidity gaps on both sides of the interaction point and two b-jets in the central region, the Higgs boson gives rise to a peak in the missing mass spectrum. The exclusive double Pomeron exchange reaction is depicted in Fig. 2.2.

The missing mass, i.e. the mass of H, can be calculated from the 4-

momenta of the incoming and outgoing protons by usint formula

$$MM^2 = (p_1 + p_2 - p_3 - p_4)^2, \qquad (2.23)$$

where p_1 and p_2 are the 4-vectors of the incoming protons and p_3 and p_4 the 4-vectors of the outgoing protons. If the protons have small transverse momentum

$$p_t^2 = p_x^2 + p_y^2 \qquad (2.24)$$

after the collision, then the missing mass can be approximated by

$$MM^2 = \xi_1 \xi_2 s, \qquad (2.25)$$

where s is the square of the center-of-mass collision energy (14 TeV at the LHC) and $\xi_{1,2}$ the momentum losses of the protons.

It has been proposed that by utilizing the missing mass method, the Higgs boson mass can be measured to an accuracy of $\mathcal{O}(1 \text{ GeV})$ per event [10], whereas the direct measurement of the Higgs mass via its decay products in $H \to b\bar{b}$ results in a mass resolution of only about $\mathcal{O}(10 \text{ GeV})$ per event. There exist a wide range of predictions for the cross section for diffractive Higgs production ranging over many orders of magnitude [11]. Probably the best estimate for the cross section of exclusive central diffraction is calculated in Ref. [10]; the authors predict the cross section of this particular reaction at the center-of-mass collision energy $\sqrt{s} = 14$ TeV to be

$$\sigma(pp \to p + H + p) \simeq 3fb \qquad (2.26)$$

for the production of a Standard Model Higgs with a mass of 120 GeV. The signal-to-background ratio for the same reaction would be

$$\frac{\text{Signal}}{\text{Background}} \simeq 3, \qquad (2.27)$$

which is 100 times larger than the signal-to-background ratio for the inclusive reaction $pp \to HX$, $H \to \gamma\gamma$. However, all experimental aspects are supposed to have been taken into account in the calculations of signal-to-background value for the inclusive reaction, which is not case for the exclusive process.

Chapter 3

LHC and beam optics

The event rate R in a collider is proportional to the interaction cross section σ_{int}. The factor of proportionality is called the luminosity $\mathcal{L}$:

$$R = \mathcal{L}\sigma_{\mathrm{int}}. \tag{3.1}$$

If two bunches containing n_1 and n_2 particles collide with a frequency f, then the luminosity is

$$\mathcal{L} = f\frac{n_1 n_2}{4\pi\sigma_x\sigma_y} \tag{3.2}$$

where σ_x and σ_y characterize the Gaussian transverse beam profiles in the horizontal and vertical directions, respectively. The LHC will be the highest luminosity accelerator with luminosity of $\mathcal{L} = 10^{34}$ cm^{-2}s^{-1} and the highest energy machine with center-of-mass energy $\sqrt{s}$=14 TeV.

3.1 Machine layout

The LHC machine consists of eight bending arcs separated by eight insertions [12]. The arcs are part of the ring occupied by regular half-cells with three dipoles and a quadrupole. Sextupoles and decapoles are located in the shadow of the dipole magnet ends. Each of the eight arcs is composed of 23 arc cells, giving a total arc length of 2456.160 m. All arc cells are made of two identical half-cells. An insertion is the part of a ring between two arcs. It consists of one dispersion suppressor, one full straight section, and a second suppressor. The straight sections are numbered as IP1, IP2,..., IP8 and the interaction points (IP) are in those straight sections at IP1, IP2, IP5 and IP8.

Dipole fields are the proper fields to bend particle beams. The purpose of quadrupoles is to keep the particle beam together and to generate specifically desired beam properties at selected points along the beam transport line, e.g. the strong focusing at the interaction point to obtain a high luminosity. Higher order poles are used as correctors.

3.2   Beam optics

To describe the motion of particles in the accelerator storage ring, a rotating coordinate system is used. The coordinate system is defined such that the x-axis is in the horizontal plane, the y-axis in the vertical plane and the z-axis is taken to be parallel with the beam pipe. The positive x-axis points to the outside of the ring and the positive y-axis points upwards. The direction of a particle track after the collision is defined by the polar angle θ and the azimuthal angle ϕ. Here θ is the angle between the particle momentum vector and the z-axis, i.e.

$$\theta = \arctan\left(\frac{\sqrt{p_x^2 + p_y^2}}{p_z}\right), \tag{3.3}$$

and its projection onto the x-axis is

$$\theta_x = \arctan\left(\frac{p_x}{p_z}\right). \tag{3.4}$$

The azimuthal angle ϕ is measured around the z-axis

$$\phi = \arctan\left(\frac{p_y}{p_x}\right). \tag{3.5}$$

The differential equation of motion in the transverse plane is given by

$$u'' + k(z)u = 0, \tag{3.6}$$

where u stands for x or y and $k(z)$ is an arbitrary function of z resembling the particular distribution of focusing along the beam line. The solution for Eq. (3.6) [13] is

$$u(z) = \sqrt{\epsilon}\sqrt{\beta(z)}\cos(\phi(z) + \phi_0). \tag{3.7}$$

The parameter function $\beta(z)$ is called the betatron function. In the interaction point, the betatron function is commonly denoted as β^* and its derivative vanishes in the IP. Above, ϵ is called emittance and it describes the beam quality and the $\phi(z)$ is a phase function given by

$$\phi(z) = \int_0^z \frac{dz}{\beta(z)} + \phi_0. \tag{3.8}$$

The beam width $\sigma_{x,y}^{\mathrm{beam}}(z)$ at any position z along the beam line is related [14] to the beam divergence $\sigma_{\theta_{x,y}}^*$ and the beam width $\sigma_{x,y}^*$ at the interaction point according to

$$\sigma_x^{\mathrm{beam}}(z) = v_x(z) \cdot \sigma_x^* \oplus L_x^{\mathrm{eff}}(z) \cdot \sigma_{\theta_x}^* \oplus \xi_0 \cdot D(z), \tag{3.9}$$

$$\sigma_y^{\mathrm{beam}}(z) = v_y(z) \cdot \sigma_y^* \oplus L_y^{\mathrm{eff}}(z) \cdot \sigma_{\theta_y}^* \tag{3.10}$$

where $L_{x,y}^{\mathrm{eff}}(z)$ is the effective length and $v_{x,y}(z)$ the magnification along the beam line. In Eq. (3.9), $D(z)$ denotes the dispersion which determines the offset from the reference trajectory. Above, $L_{x,y}^{\mathrm{eff}}(z)$ and $v_{x,y}(z)$ depend on the betatron phase advance $\Delta\mu(z) = \int \beta^{-1}(z)dz$ via the following relations:

$$L_{x,y}^{\mathrm{eff}}(z) = \sqrt{\beta_{x,y}(z)\beta^*} \sin \Delta\mu(z) \tag{3.11}$$

$$v_{x,y}(z) = \sqrt{\frac{\beta_{x,y}(z)}{\beta^*}} \cos \Delta\mu(z). \tag{3.12}$$

The value of the beam divergence $\sigma_{\theta_{x,y}}^*$ at the interaction point is given by

$$\sigma_{\theta_{x,y}}^* = \sqrt{\frac{\epsilon}{\gamma\beta^*}}, \tag{3.13}$$

and the beam width $\sigma_{x,y}^*$ at the interaction point is

$$\sigma_{x,y}^* = \sqrt{\frac{\epsilon}{\gamma}\beta^*} \tag{3.14}$$

where ϵ is the normalised emittance and β^* is the betatron amplitude at the interaction point.

The trajectory of a proton in the transverse plane at a given position z along the beam line can be expressed using the initial conditions $((x^*, y^*)$ and $(\theta_x^*, \theta_y^*))$ at the interaction point via

$$x(z) = v_x(z) \cdot x^* + L_x^{\mathrm{eff}}(z) \cdot \theta_x^* + \xi \cdot D(z) \tag{3.15}$$

$$y(z) = v_y(z) \cdot y^* + L_y^{\mathrm{eff}}(z) \cdot \theta_y^*. \tag{3.16}$$

3.3 Low/High β^* running

The nominal operation of the LHC, optimised for maximum luminosity, will use strong focusing at the interaction points. The nominal optics mode is called the low β^*-mode, which refers to the low value of the betatron function β^* at the interaction point. The smallest β^* value is limited by triplet magnet aperture to β^*=0.5 m. In the low β^*-mode the transverse beam size is small, which increases the luminosity. After the first years of

Table 3.1: LHC parameters for the low and high β^* operation.

Parameter	Low $\beta^* = 0.5$ m	High $\beta^* = 1100$ m
Number of bunches	2835	36
Bunch spacing	24.95 ns	2.5 μs
Luminosity L (cm^{-2}s^{-1})	10^{34}	10^{28}
Transverse normalized emittance (μm rad)	3.75	3.75
Transverse beam size $\sigma^*_{x,y}$ at IP (μm)	16	740
Beam divergence $\sigma^*_{\theta_{x,y}}$ at IP (μrad)	31.7	0.67
Crossing angle (μrad)	2×150	0

LHC operation the optimised luminosity will reach 10^{34} cm^{-2}s^{-1}. In order to avoid unwanted parasitic encounters at low β^*-mode, the beams cross at an angle of 2·150 μrad. More design parameters for the low β^*-mode are given in the left column of Table 3.1.

At the beginning of LHC operation there will be short dedicated runs with high β^* -mode. For the design parameters, see right column of Table 3.1. During high β^* operation, the total cross section and the elastic scattering can be measured by TOTEM [15].

Chapter 4

Detectors

4.1 CMS

The Compact Muon Solenoid (CMS) detector [16] has been designed to cleanly detect diverse signatures from new physics by identifying and precisely measuring muons, electrons, taus, photons, jets and missing transverse energy over a large energy range and at high luminosity. The detector tracking and calorimetry components are to be built within a high-field (4T) superconducting solenoid, leading to a compact design for the muon spectrometer. The magnetic flux is returned via an iron yoke which is instrumented with muon stations.

The goal of the central tracking system is to reconstruct isolated high p_t tracks and high p_t tracks within jets. It consists of silicon pixel detectors, placed close to the interaction region. The electronic readout is focusing on an analogue design yielding a good position resolution of 15 μm in both coordinates. Next come the silicon microstrip detectors, which are able to withstand the radiation fluences expected over ten years use of LHC. The tracking system can cover the pseudorapidity range $|\eta| < 5.0$.

The task of the electromagnetic calorimeter is to identify and precisely measure the energies and locations of electrons and photons. The electromagnetic calorimeter is split into barrel and end-cap sections to surround the collision point of the interacting protons. It consists of around 118,000 lead tungstate crystals out of which about 25,000 are in the end-caps.

A hadron calorimeter with copper absorbers will be installed between the electromagnetic calorimeter and the coil. It plays an essential role in the identification and measurement of quarks, gluons, and neutrinos by measuring the energy and direction of jets and of missing transverse energy flow in events. Scintillator tiles equipped with wavelength-shifter fibers are used as detecting elements.

The very forward calorimeter improves the measurement of missing transverse energy and enables very forward jets to be identified. It covers the
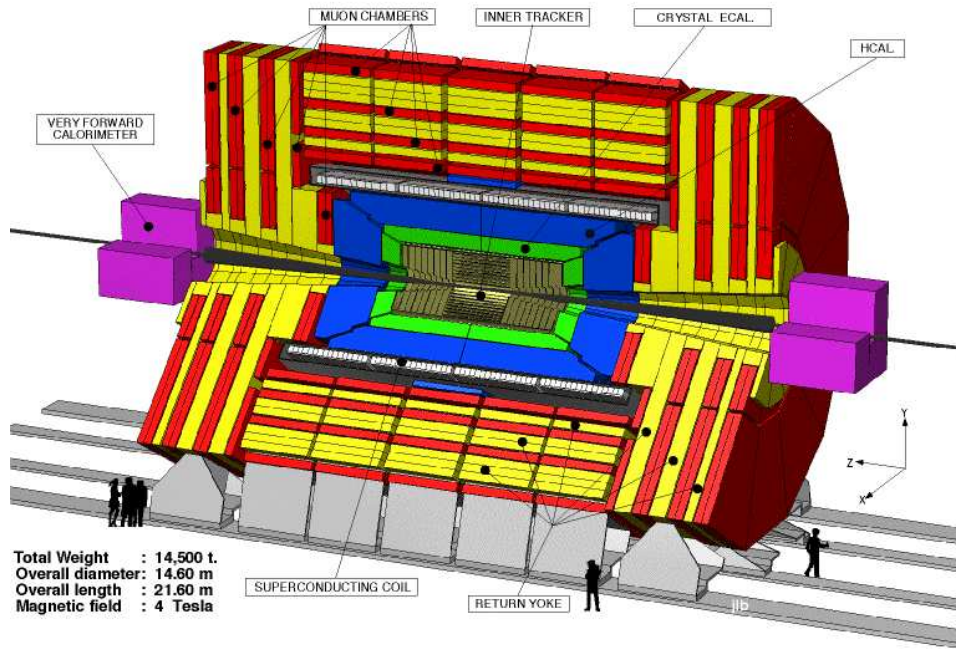
Figure 4.1: Overview of the CMS detector.

pseudoradidity range $3.0 \leq |\eta| \leq 5.0$.

Muons are identified in four separate stations, each consisting of several planes of drift chambers, inserted in the barrel part of the solenoid return yoke. Each station will also contain triggering planes made of resistive plate chambers. In the barrel region as well as in the endcaps the momentum is measured three times: inside the inner tracking volume, just after the coil, and in the flux return.

For the nominal LHC design luminosity of 10^{34} cm^{-2}s^{-1}, an average of 20 inelastic events occur every 25 ns, the beam crossing time interval. This input rate of 10^{9} interactions per second must be reduced by a factor of at least 10^{7} down to 100 Hz. The reduction of the event rate has been choosen to be done in two steps. The Level-1 trigger system operates on a subset of the data collected from each LHC beam crossing. The processing has no deadtime and the decision to collect the full set of data relating to a given crossing is taken after a fixed latency of 3 μs. The Level-1 trigger consists of the trigger chambers of the muon spectrometer and the calorimeter and global trigger. The output rate from Level-1 is estimated to be around 100 kHz.

After a positive Level-1 trigger decision, the filter farm performs event selection in progressive stages by applying a series of High Level Trigger filters. Much information is not available on the time scale of the Level-1

trigger decision. This information, including information from the tracker and the full granularity of the calorimeters, is then used by in the High Level Triggers. Eventually, the High Level Triggers use the full event data for the decision to keep the event [17].

4.2 Very forward detectors

Good detector acceptance at small angles to the beam direction is essential for studies of hadronic diffraction. The detector system has to be capable of seeing both the leading protons at a very small angle. In terms of pseudorapidity, the detector system has to be able to measure protons with $|\eta| \approx 10$. This forward region is not covered by CMS, or any other base line designs of the main experiments at LHC. Therefore, an extension of acceptance coverage in the forward direction is necessary for studies of diffractive scattering.

In order to measure leading protons before they hit the beam pipe walls, their trajectories have to be tracked inside the beam-pipe close to the beam, far from the interaction point. Being close to the beam, detectors have to work in an intense radiation environment and the amount of space available is constrained. The detectors have to be integrated with the machine requirements. Changing machine conditions require movable detectors.

4.2.1 Microstation

The microstation [18] design consists of a detector unit which is assembled on the beam pipe. The unit includes moving sensor planes with their support, and a cooling system inside a vacuum chamber welded to the beam pipe. The vacuum chamber has feed-throughs for the electronics and the cooling system.

The microstations will be implemented with two planes of sensors moving along the x-axis to approach the beam. The movement is based on piezo-electric deformation of a ceramic material. The detectors are suspended on the slides of two linear stepping motors mounted side by side. A simple linear guide at the bottom, consisting of a thin blade moving in an axial slot, prevents rotation around the stator shaft. A cooled silicon detector technology is considered as the main implementation option, possibly including the use of oxygenated silicon sensors.

The microstation is a novel concept and its development was initiated with the Finnish State Reseach Centre (VTT). The advantages of microstations are that they are compact and light detector systems. Their geometry and materials are compatible with the machine requirements and they will be integrated with the beam vacuum chamber.

4.2.2   Roman Pot

Roman Pots are stainless steel containers that allow the detectors to function close to the beam but outside the machine vacuum. Particles traverse thin steel windows at the entrance and exit of each pot. The pots are remotely controlled and can be moved close to the beam during stable beam conditions and retracted otherwise [14]. Forward detectors in Roman Pots have been added to many experiments, for example in H1 and ZEUS at HERA and CDF and D0 at the Tevatron.

While Roman Pots are an established technology, they cannot be easily integrated with the designed or already existing accelerator magnet lattice. Since the Roman Pots are operated in atmospheric pressure, the acceptance and distance to the beam is not always optimal [19].

Chapter 5

Simulation chain

For exclusive central diffractive events, the propagation of produced leading protons and possible inaccuracies influencing the reconstruction of their kinematics were simulated in four parts. The events were generated with the PHOJET and PYTHIA event generators and then the inaccuracies at the interaction point were taken into account. Propagation of leading protons along the beam line was performed with MAD and finally the behaviour of the detectors was simulated.
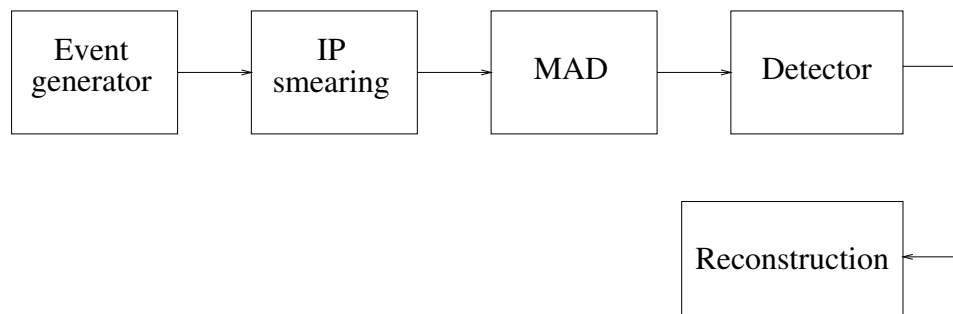
Figure 5.1: Schematic figure of the simulation chain.

5.1 Event generator

Proton-proton collisions were simulated with PHOJET [20]. It is a Monte Carlo (MC) event generator, which can be used to simulate hadronic multi-particle production at high energies for hadron-hadron, photon-hadron, and photon-photon interactions. The ideas and methods used in the program are based mainly on the phenomenological Dual Parton Model (DPM, for a review see Ref. [21]) combined with perturbative QCD. Low-p_t interactions, such as central diffraction, are modelled on the basis of Regge theory. The

main types of applications of PHOJET are cross section calculations and generation of hadronic final states by MC. In this study, PHOJET was set to produce only pp collisions with exclusive central diffraction ($pp \rightarrow p + X + p$).

The central system particle X is unstable and subsequently decays into the observable, stable ones. The decays of X ($X = H \rightarrow b\bar{b}$) were simulated with PYTHIA [22], which is a frequently used event generator in high-energy physics. PYTHIA provides the generation of common interactions between elementary particles such as electrons, positrons, protons and antiprotons, following to interactions and decays of outgoing particles. However, central diffractive processes are not available in PYTHIA and therefore it was only used for the decays of X [23]. PHOJET had no Higgs decay implemented.

5.2   IP Smearing

In real particle collisions, the coordinates of the interaction point (IP), the angle between leading protons and the beam line (θ) and the beam energy are never known exactly. In order to simulate the real conditions, the coordinates of IP were smeared with a Gaussian random function, i.e.

$$x_{\text{sim}} = \sigma_x r_x, \qquad\qquad\qquad (5.1)$$

$$y_{\text{sim}} = \sigma_y r_y, \qquad\qquad\qquad (5.2)$$

$$z_{\text{sim}} = \sigma_z r_z, \qquad\qquad\qquad (5.3)$$

where $\sigma_{(x,y,z)}$ is standard deviation of the (x, y, z) and $r_{(x,y,z)}$ is a normalized Gaussian random function. IP smearing of the z-coordinate has not been studied here, because the z-position is foreseen to determine from the tracks of the two b-jets to an accuracy of few 100 μm. The standard deviations for baseline design are shown in Table 5.1.

The smearing of the angle θ was performed by adding a Gaussian random function to the θ-value given by the physics event generator. Thus $\theta_{\text{sim}} = \theta_{\text{gen}} + \sigma_\theta r$. The smearing of the angle θ is also called beam divergence.

The uncertainty of the leading proton energy depends linearly on the uncertainty of the beam energy. The effect has been taken into account by multiplying the energy given by the event generator by a Gaussian number, whose expectation value is 1. Thus the simulated energy of leading protons is calculated as $E_{\text{sim}} = E_{\text{gen}}(1 + \sigma_E r)$. Here σ_E is also called beam energy spread.

In addition, the beam divergence and the beam energy spread affect the momentum components, which are calculated with simple geometry from simulated angle and energy. The formulas for momentum components are

$$p_x = E_{\text{sim}} \sin(\theta_{\text{sim}}) \cos(\phi), \qquad\qquad\qquad (5.4)$$

$$p_y = E_{\text{sim}} \sin(\theta_{\text{sim}}) \sin(\phi), \tag{5.5}$$

$$p_z = \frac{E_{\text{sim}}}{\sqrt{1 + \tan^2(\theta_{\text{sim}})}}. \tag{5.6}$$

Table 5.1: Overview of baseline IP parameters.

$\sigma_{x,y}$	σ_z	$\sigma_{\theta_{x,y}}$	σ_E
16 μm	5 cm	30 μrad	10^{-4}

5.3   Beam optics simulation

The trajectories of the scattered protons were simulated with MAD (Methodical Accelerator Design) [24]. MAD is a tool for charged-particle optics in alternating-gradient accelerators and beam lines. In other words, MAD simulates how various accelerator structures affect the beam particles in the beam pipe. It can handle both very large and very small accelerators, and solve various problems on such machines. In this study, MAD was set to use the LHC optics version 6.2 [25]. The inaccuracy of magnetic element alignment and the deviation of magnetic field strength can also be taken into account in MAD.

After each accelerator element, we checked whether the proton had hit the beam pipe wall or not. The beam pipe was approximated to be a circle with 3.0 cm radius. If the path of the proton was not inside the circle, the position where the proton was lost was stored for further investigations.

5.4   Detector simulation

In a case when the proton has not hit the beam pipe wall before the detector location, the next step is to study whether the detector is able to register the particle. For particles with small momentum loss ξ, the limiting factor is how close to the beam leading protons can be measured. This boundary is given by

$$\Delta = k \cdot \sigma(z) + \delta, \tag{5.7}$$

where $\sigma(z)$ is the beam size at the given location, k is the dimensionless approach of the detector to the nominal beam position and δ is the detector dead space. Thus $k \cdot \sigma(z)$ describes how near to the beam the detector can be placed as a multiple of beam size at a given location. The detector dead

Table 5.2: Overview of detector parameters used.

	detector resolution	beam position resolution		beam position offset	detector offset
σ_x	10 μm	5 μm	c	10 μm	-10 μm

space approximates the region within which the detector cannot register particles. It consists of the radiation shielding and the dead space of the detector itself. In the baseline simulations $10\sigma_z$ approach and 0.1 mm dead space have been used. The chosen baseline values might be somewhat too optimistic. The size and the shape of the beam pipe before the detector position and the size of the detector determine the upper bound on ξ for the measured protons with large ξ value.

The inaccuracy of the detectors in measuring the position of protons was taken into account by smearing the detector coordinates. The coordinates were smeared by adding to them a Gaussian random function as described in Section 5.2, i.e. $x_{\text{real}} = x_{\text{sim}} + \sigma_x r$, were σ_x is standard deviation of the x and r is a normalized Gaussian random function. All the coordinates are smeared independently of each other and this effect is called detector resolution. No specific detector implementation (e.g. strip or pixel detector) has been used.

The beam position is not known exactly either. Consequently, this effect was taken into account by smearing coordinates of the protons by adding to them a Gaussian random variable as described above. In one detector location, the coordinates measured in two different stations are smeared by adding to them the same Gaussian random variable.

The proton beam is not exactly in the middle of the beam pipe. Consequently, the absolute distance between the detector and nominal beam position is not precisely known. This beam offset was simulated by adding a constant in the coordinates at both stations, i.e. $x_{\text{real}} = x_{\text{sim}} + c$, where c is the offset.

Detector misalignment was taken into account by adding a constant number in the coordinates only at the second station at one detector location.

Chapter 6

Momentum reconstruction

The basic principle of reconstructing the proton momentum is to find a direct way to calculate the kinematic variable ξ (momentum loss) or $\theta_{x,y}^*$ (projection of polar angle) from the measured coordinates of the leading protons. The mass of the central system can then be calculated by using the missing mass method.

In order to measure leading protons before they hit the beam pipe wall, their trajectories have to be tracked inside the beam pipe close to the beam far from the interaction point. Since the approach of the detector to the nominal beam position is limited, protons with small ξ cannot be detected in the same location as protons with larger ξ, see Section 7.1. Therefore, we have chosen three different detector locations: 215 m, 308 m and 420 m from the interaction point. At the 215 m and 420 m detector locations, the trajectories of the protons are measured at two detector stations separated by 10 m. There are no magnetic elements between the two stations and thus the projections of the polar angle $\theta_{x,y}$ at these locations can be calculated using simple geometry from the measured coordinates at the two stations. The two observables in ξ reconstruction are x_{215} and $\theta_{x,215}$ at the 215 m location and x_{420} and $\theta_{x,420}$ at the 420 m location.

At the 308 m location, there is not enough space for two detector stations. The trajectories of leading protons are measured at 308 m and 338 m from the IP, two dipole magnets between them. In the reconstruction of ξ, the two observables used are the coordinates x_{308} and x_{338}. Previous studies have shown that only one observable, e.g. x, is insufficient for precise ξ reconstruction at all the three locations.

6.1 Coordinate transformation

Figure 6.1 shows the distribution of leading protons measured at the 420 m and 430 m locations. In the upper plot, each colour corresponds to a 0.0005 range in ξ-values, and in the lower plot each colour corresponds to a 28 μrad

range in θ_x^*. The smallest ξ value, ξ=0.002, lies in the top right corner of the distribution while the largest ξ value, ξ=0.015, lies in the bottom left corner of the distribution.

As can be seen in Fig. 6.1, different ξ values are well separated if both coordinates are known. In other words, a certain pair of the measured observables corresponds to a certain ξ value as well as a certain θ_x^* value. Hence ξ and θ_x^* can be reconstructed from the two measured observables independently of each other.

There prevails a strong correlation between the two observables in all three locations. In order to spread the data (and to produce more accurate results), a coordinate transformation was made. The coordinate transformation was performed by making a profile[1] plot of the aforementioned plot, fitting a linear function in the profile plot and then choosing a vector parallel with the linear function and a vector orthogonal to the linear function as transformed coordinates. The same distribution as in Fig. 6.1 is displaced in these transformed coordinates in Fig. 6.2. The coordinate transformation preserves the separation of different ξ and θ_x^* values.

6.2 Momentum reconstruction with 3-dimensional fitting

At the 308 m and 420 m locations the parametrisation $\xi_{\mathrm{calc}} = f(x', y')$ was carried out with a 3-dimensional fitting. With the parametrisation estimate ξ_{calc} can be calculated for all pairs of transformed coordinates (x', y'). Parametrisation for ξ reconstruction was preferred due to the efficiency of computing.

6.2.1 Reconstruction at the 308 m location

At the 308 m location, coordinates were transformed according to

$$x' = x_{338} - 3.2522x_{308}$$
$$y' = x_{338} + 3.2522x_{308}.$$
(6.1)

For determining parametrisation, we defined the average ξ for a given set of (x', y'). In the basis of the transformed coordinates (x', y'), the distribution was projected onto a 2-dimensional histogram and the histogram bins were filled with normalized ξ-values. Normalization was done by dividing the ξ-weighted number of hits by the total number of hits in a bin.

The 2-dimensional ξ-weighted histogram was plotted as a 3-dimensional lego plot, in which the height of bars corresponds to the normalized, i.e.

---

[1]In a profile plot the horizontal axis is divided into a certain number of bins. Each bin is given the average value of the variables in that bin and the error bars indicate the spread.
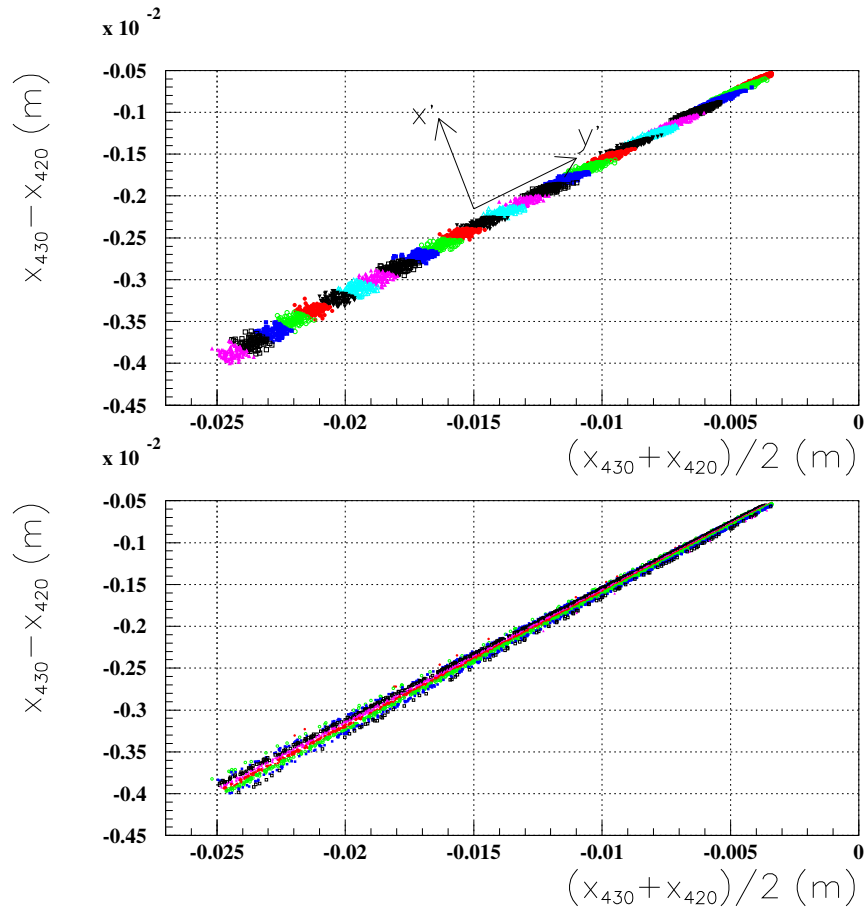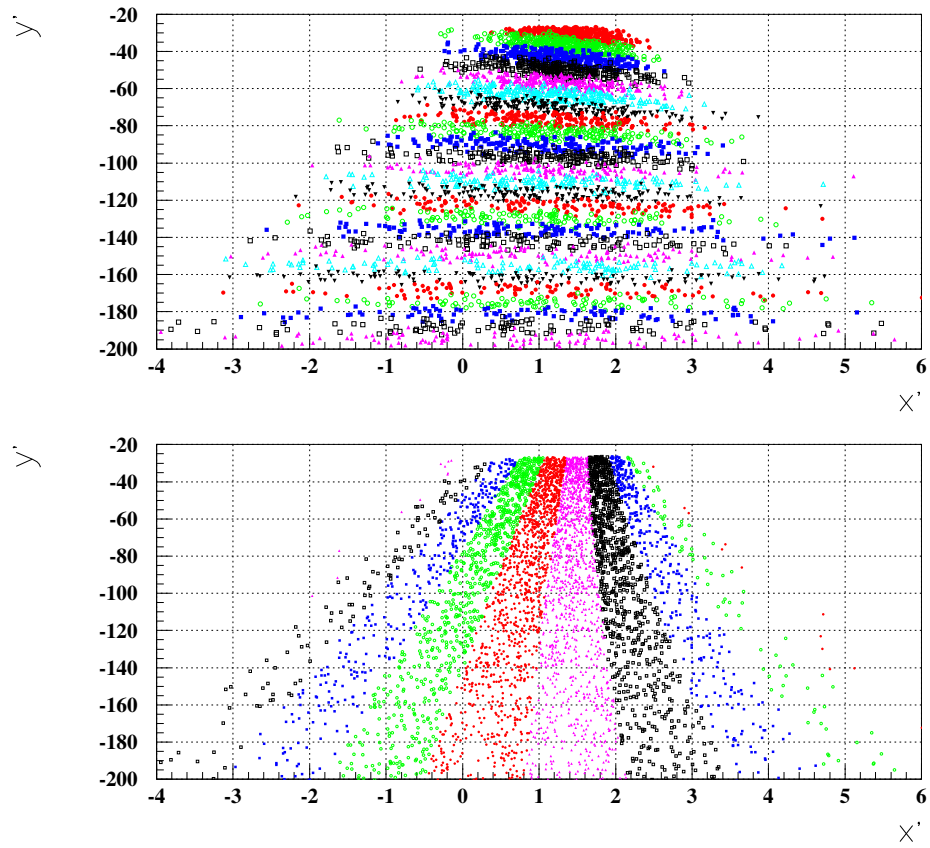
Figure 6.1: Distribution of protons measured at the 420 m location. In the upper plot each colour corresponds to a ξ range $|\xi_{\mathrm{max}}-\xi_{\mathrm{min}}|=5\cdot10^{-4}$ while in the lower plot each colour corresponds to a θ_x^* range $|\theta_{x,\mathrm{max}}^*-\theta_{x,\mathrm{min}}^*|=28\,\mu$rad.

Figure 6.2: Distribution of protons measured at the 420 m location after coordinate transformation. In the upper plot each colour corresponds to a ξ range $|\xi_{\max} - \xi_{\min}|$=5·$10^{-4}$ while in the lower plot each colour corresponds to a θ_x^* range $|\theta_{x,\max}^* - \theta_{x,\min}^*|$=28 μrad.
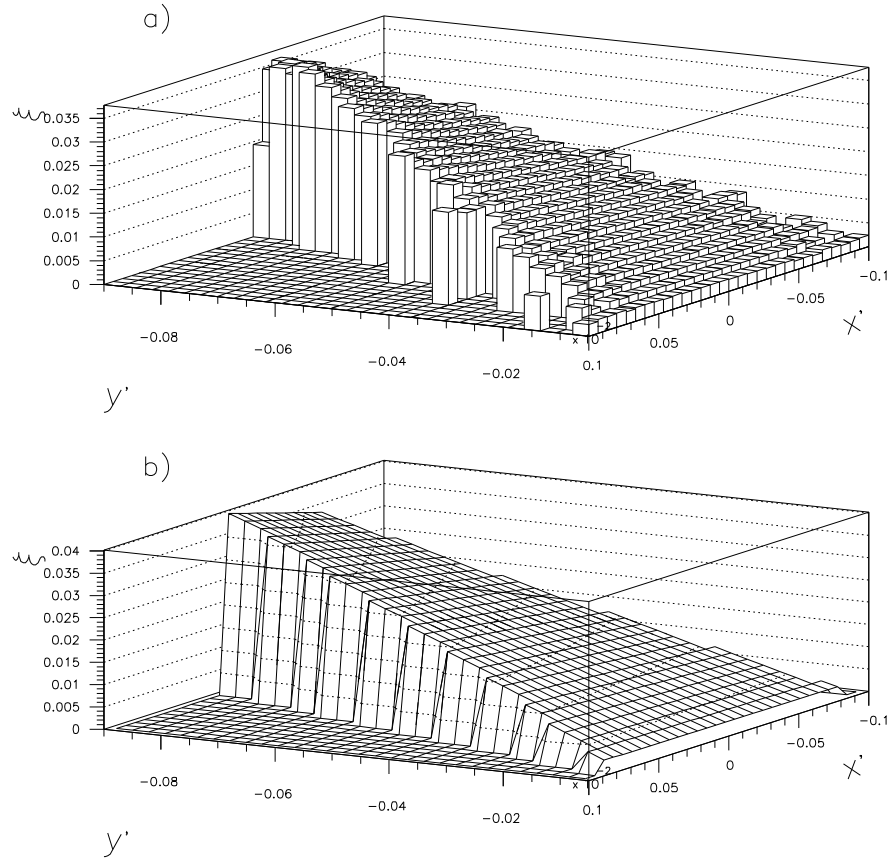
Figure 6.3: a) The 3-dimensional lego plot of normalized ξ values at the 308 m location and b) the fitted surface.

averaged ξ-value. The 3-dimensional lego plot is depicted in Fig. 6.3a. To these average values, a surface $f(x', y')$ was fitted. Before fitting most of the empty bins were excluded and the fitting was performed only in a restricted area. The fitted surface can be seen in Fig. 6.3b.

Many different kinds of functions were studied for the surface fitting. For reconstructing the ξ using the measured coordinates at the 308 m location the function

$$\xi_{calc}^{308}(x', y') = c_1 \sin(x') + c_2 \sin(y') + c_3 x' + c_4 y' + c_5 x' y' + c_6 \qquad (6.2)$$

proved to yield the best results. In Eq. (6.2), x' and y' are the transformed coordinates according to Eq. (6.1) and the c_n are constants from the fit.

The reconstruction was improved by fitting two separate surfaces of the

form (6.2) on the lego plot. Further small scale improvements were done by plotting the absolute error between ξ and ξ_{calc} as a function of the transformed coordinates. The dependence of the transformed coordinates was corrected with a correction function, which was subtracted from the surface equation. The correction functions were second and third order polynomials of the transformed coordinates. The results of the reconstruction are discussed in Section 6.4 and a more precise description of the 3-dimensional fitting for the 308 m location is given in Ref. [26].

6.2.2 Reconstruction at the 420 m location

The method to reconstruct ξ from the observables at the 420 m location was performed in a way similar to that for the 308 m location. The transformed coordinates

$$
\begin{aligned}
x' &= 250783\theta_{x,420} - 4321x_{420} + 1 \\
y' &= 250783\theta_{x,420} + 4321x_{420}
\end{aligned}
\tag{6.3}
$$

were chosen and the function

$$
\begin{aligned}
\xi_{calc}^{420}(x', y') = a_1 x'^3 + a_2 y'^3 + a_3 x'^2 y' + a_4 x' y'^2 + a_5 x'^2 + a_6 y'^2 \\
+ a_7 x' y' + a_8 x' + a_9 y' + a_{10}
\end{aligned}
\tag{6.4}
$$

for surface fitting proved to yield the best results. The reconstruction was improved by fitting three separate surfaces of the form (6.4) on the 420 m lego plot. For a more precise discussion about the reconstruction from the observables at the 420 m location, see Ref. [27].

6.3 Momentum reconstruction with linear interpolation

However, at the 215 m location 3-dimensional fitting is not sufficient to enable the reconstruction well enough. The dispersion at the 215 m location is smaller compared to the dispersion at the 308 m and the 420 m locations, which causes different ξ-values not to be as clearly separated. Instead of 3-dimensional fitting, a two-dimensional grid with linear interpolation was used. In order to achieve better accuracy for the reconstruction with this grid, a coordinate transformation

$$
x^* = \frac{0.5}{x + 0.005} + \frac{0.5}{\theta_x + 0.001}
\tag{6.5}
$$

$$
y^* = 0.58458 \cdot 10^{-2}x - \theta_x
\tag{6.6}
$$

was introduced for clockwise moving protons. The coordinate transformation for anticlockwise moving protons was similar except that the constant coefficient 0.58458 in the definition of y^* was shifted to 0.42929.

The grid was constructed of 300 000 events in such a way that the range considered along the x^*- and y^*-axis was divided into intervals of equal size. Each grid point was given the average ξ-value in that bin. Let the sequence $a_1, a_2, ...$ be the tabulated values of x^* and the sequence $b_1, b_2, ...$ the tabulated values of y^*. If there exists subscripts i and j (i and j run through the grid points) for input values x^* and y^*, such that $a_i \leq x^* \leq a_{i+1}, b_j \leq y^* \leq b_{j+1}$, the following algorithm was carried out

$$
\begin{aligned}
t &= (x^* - a_i)/(a_{i+1} - a_i) \\
g_j &= (1 - t)f(a_i, b_j) + tf(a_{i+1}, b_j) \\
g_{j+1} &= (1 - t)f(a_i, b_{j+1}) + tf(a_{i+1}, b_{j+1}) \\
u &= (y^* - b_j)/(b_{j+1} - b_j) \\
f_{\text{appr}} &= (1 - u)g_j + ug_{j+1}.
\end{aligned}
\tag{6.7}
$$

The vector $f(a_i, b_j)$ consists of the averaged ξ values at the fixed grid point (a_i, b_j).

6.4 Accuracy of reconstruction

The correctness of the reconstruction methods was examined by studying the relative error, i.e.

$$
\frac{\xi - \xi_{\text{calc}}}{\xi}.
\tag{6.8}
$$

The relative error as a function of ξ is shown in Fig. 6.4 for clockwise moving protons and in Fig. 6.5 for anticlockwise moving protons. As can be seen in the figures, the relative spread for all detector locations at both sides is of the order of 0.002. The spread for the 308 m and 420 m methods is slightly dependent on ξ. The reconstruction methods for the 215 m location can reproduce ξ without systematic shift in the relative error, but the methods for the 308 m and 420 m locations affect some systematic ξ dependent shift on the reconstructed ξ_{calc} values.

Linear interpolation, which is used for the 215 m location, produces a smoother distribution of relative error than the 3-dimensional fitting. However, linear interpolation is computationally tougher than 3-dimensional fitting and the analytical formula $f(x', y')$ for calculating the recostructed ξ value was preferred. If needed, the 3-dimensional fitting method could be improved by calculating average ξ of more than 20 000 events, which were used here, and optimising the form of the surface. Linear interpolation can
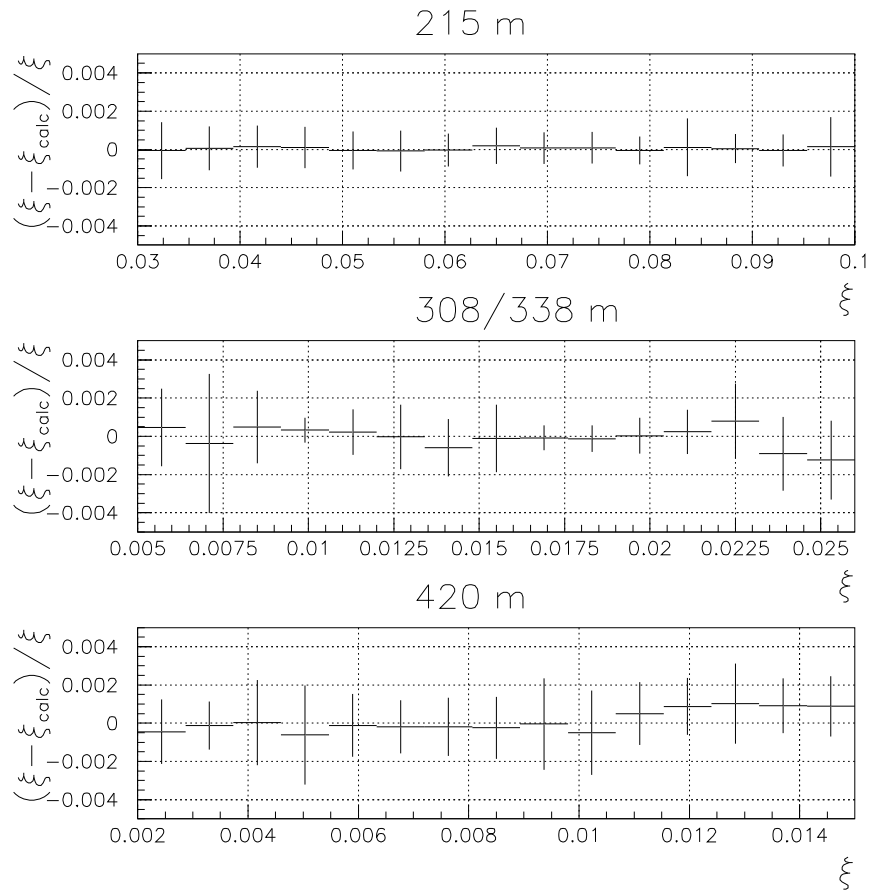
Figure 6.4: Relative error of the ξ reconstruction method for clockwise moving protons.

also be used for the 308 m and 420 m locations and for the 215 m location it could be improved by using more events for grid construction.

The relative error caused by the method used is negligible compared to the inaccuracy effects to be discussed in Ch. 7. Therefore, the accuracy of the reconstruction is clearly sufficient.
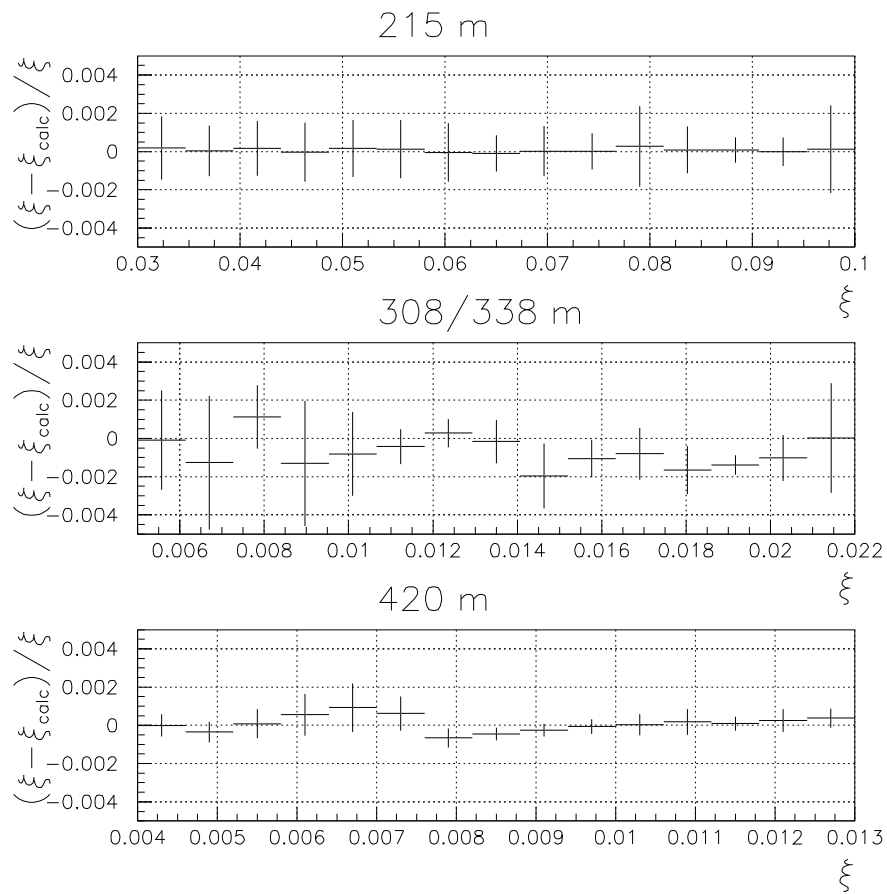
Figure 6.5: Relative error of the ξ reconstruction method for anticlockwise moving protons.

Chapter 7

Results

In this Chapter, the acceptance of the carefully selected detector locations and the accuracy of the momentum reconstruction and mass resolution due to several inaccuracies has been studied. The inaccuracies include five resolution effects and two systematic shifts. The resolution effects are detector resolution, beam position resolution, transverse beam size, angle divergence and energy spread, and the systematic shifts are absolute beam position and detector misalignment. Each inaccuracy effect is described more precisely in Ch. 5. The effects of these inaccuracies have been studied using the reconstruction methods described in Ch. 6.

The inaccuracy in the alignment of the magnetic elements and the variations of magnetic field strength with respect to nominal values will also affect the values of the reconstructed ξ. They were not studied in this thesis.

7.1   Acceptance

The detector acceptance, i.e. the fraction of scattered protons which reach the detector, depends on the area in which the detector can measure the outgoing protons. The lower limit in the ξ acceptance crucially depends on the closeness of the approach and secondly on the active size of detector. The size and shape of the beam pipe before the detector position determine the upper limit in ξ acceptance.

At 215–430 meters from the interaction point, the beam size is 80–360 μm and the baseline approach to the nominal beam position is 10σ. The acceptance for the approach of 10, 15 and 20σ with 0.1 mm dead space is shown in Fig. 7.1 with solid, dashed and dotted lines, respectively.

Detector dead space is the approximated width of radiation protection and other structures of the detector between the beam and the sensor inside the detector. It is the region within which the detector cannot register particles. In Fig. 7.2, the acceptance for 0.1 mm dead space is expressed with solid lines, for 0.5 mm dead space with dashed lines and for 1.0 mm
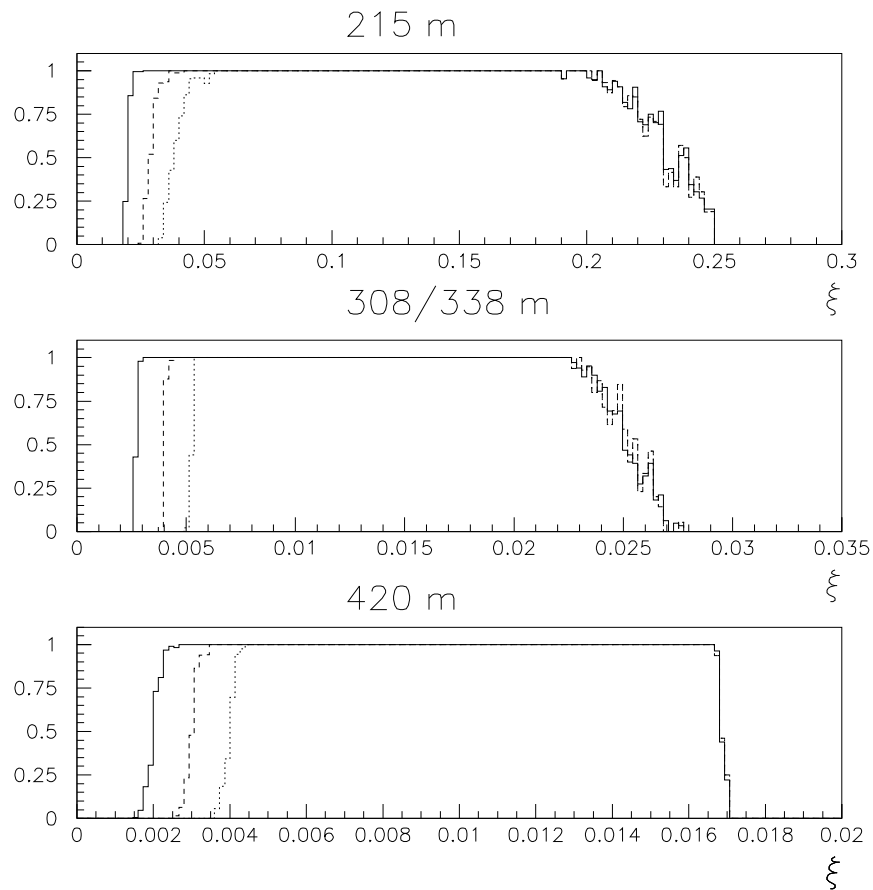
Figure 7.1: The ξ acceptance for clockwise moving protons with different detector approaches to the beam for all three detector locations. The solid lines correspond to a 10σ approach, dashed lines to a 15σ approach and dotted lines to a 20σ approach. Detector dead space is constant (0.1 mm) in all cases.

dead space with dotted lines. The approach was set to 10σ in the figure.

As can be seen in Figs. 7.1 and 7.2, it is more important to obtain the closest possible approach than small detector dead space at the 420 m location.

In the following simulations we have used a detector with 10 cm half width, 10σ approach to the beam and 0.1 mm dead space.

The detector locations were chosen such that the acceptances of different locations overlap. As can be seen from Fig. 7.3, the full acceptance from $\xi \geq 0.002$ can be covered with the three selected locations. In the figure, the solid line corresponds to the acceptance at the 420 m locations, the dashed line to the 308 m location and the dotted line to the 215 m location.

From Fig. 7.3 one can see that the acceptance is different for clockwise and anticlockwise moving protons. This is caused by a larger dispersion on the negative side of the interaction point. The dispersion affects the x coordinate of the scattered protons by displacing protons more away from the nominal beam position, see Eq. (3.15). Consequently, the detector is able to measure protons with slightly smaller ξ values but the acceptance of protons with large ξ values is decreased. The scattered protons with large ξ values hit the beam pipe before reaching the detector.

The mass acceptance of the central system is shown in Fig. 7.4, where the dotted line is the combined mass acceptance of all three detector locations, the dashed line is the combined mass acceptance of the 215 m and the 420 m locations and the solid line corresponds the mass acceptance of the 215 m location only. The mass values from where the mass acceptance is greater than 0.5 are 140 GeV, 170 GeV and 620 GeV, respectively to the aforementioned combinations. If there exist detectors only at the 215 m location, it will be able to detect protons of reactions with the mass of the central system $M \geq 300$ GeV. Therefore the Standard Model Higgs cannot be measured if there are detectors only at the 215 m location. The mass acceptance of 120 GeV central system particle will be about 40% when all three detector locations measure protons and about 35% if the 308 m location is missing. The 308 m location allows for overlap in the ξ acceptance, but the reduction in the mass acceptance for 120 GeV Higgs is only 10% if the 308 m detector location does not exist.

7.2   Resolution

The effects of resolution issues have been studied with the reconstruction methods described in Ch. 6. The particle trajectories were smeared at the IP or at the detector location and then the ξ value was reconstructed with the reconstruction method, which was derived from unsmeared data. Then the ξ value, which was reconstructed from the smeared data, was compared to the true ξ value.
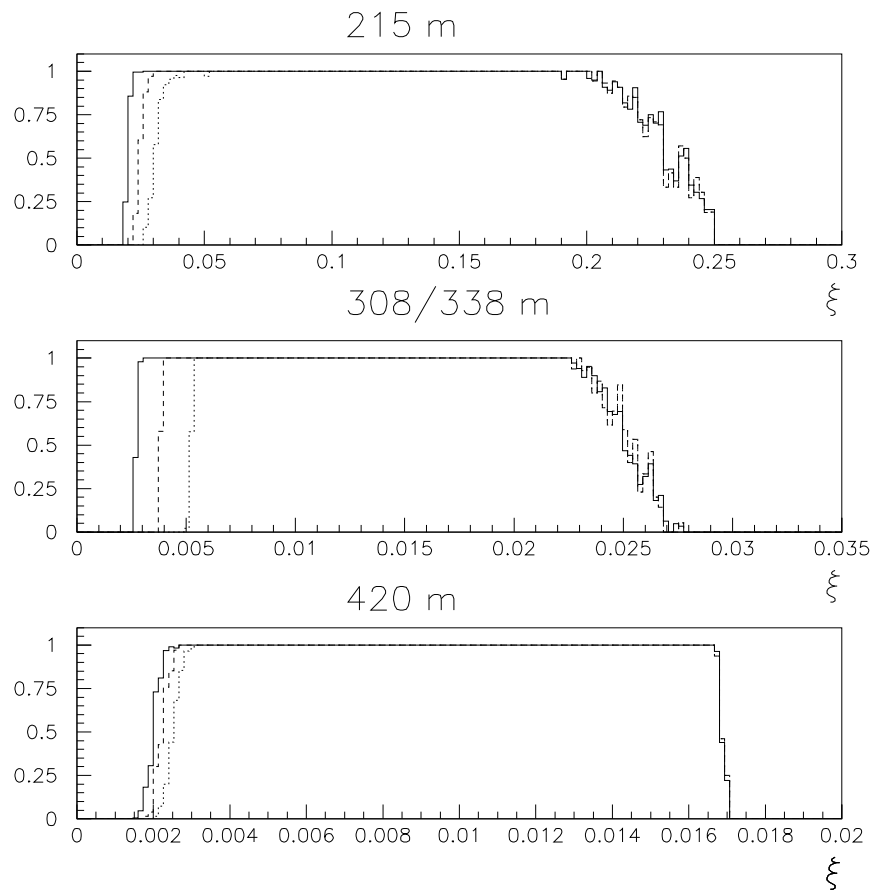
Figure 7.2: The ξ acceptance for clockwise moving protons with different detector dead spaces for all the three detector locations. The solid lines correspond to a 0.1 mm dead space, dashed lines correspond to a 0.5 mm dead space and dotted lines correspond to a 1.0 mm dead space. The approach is constant (10σ) in each case.
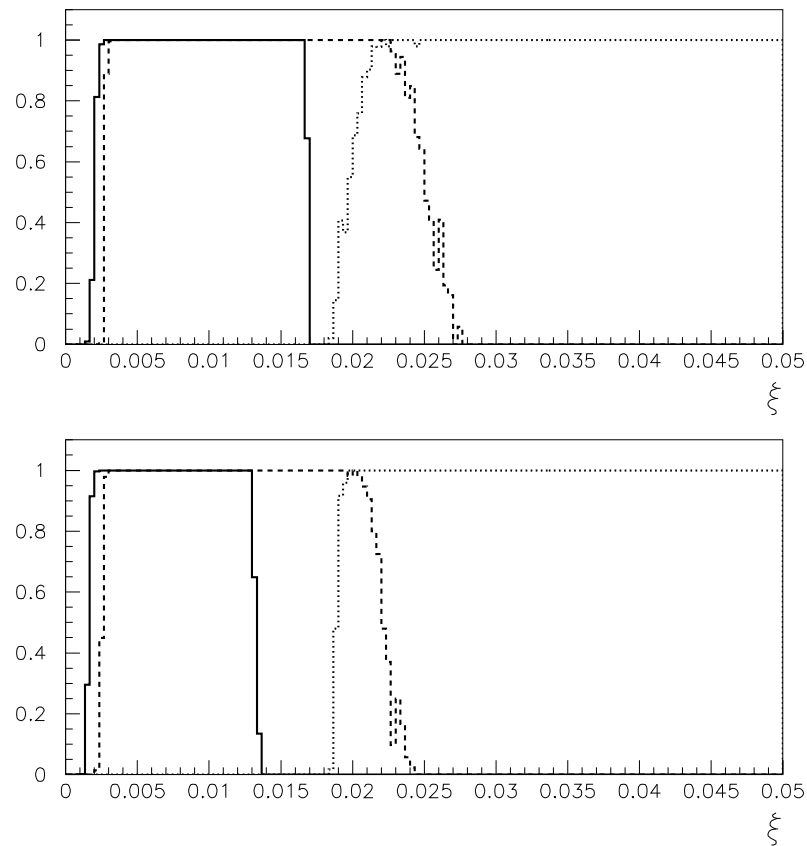
Figure 7.3: The combined ξ acceptance of all three detector locations. The solid lines correspond to the 420 m detector locations, the dashed lines correspond to the 308 m detector locations and the dashed lines correspond to the 215 m detector locations. The upper plot is the acceptance for clockwise moving protons while the lower one is the acceptance for anticlockwise moving protons.
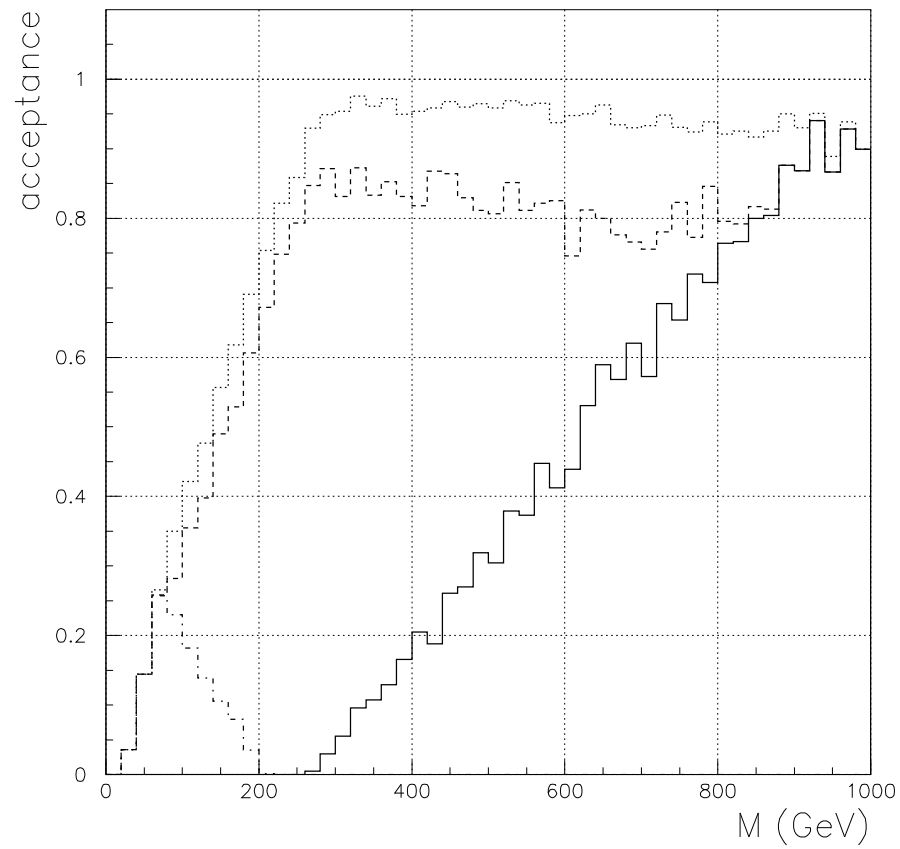
Figure 7.4: Mass acceptance for different combinations of detector locations. The solid line is the mass acceptance if there are detectors only at the 215 m locations. If only the 215 m and the 420 m detector locations exist, the mass acceptance is shown as the dashed line and the dotted line is the combined mass acceptance of all three detector locations. In the left lower corner the mass acceptance is shown for the 420 m location only.

Table 7.1: The baseline ξ acceptances for all three detector locations.

detector location	acceptance for clockwise moving protons	acceptance for anticlockwise moving protons
215 m	$0.022 \leq \xi \leq 0.2$	$0.020 \leq \xi \leq 0.2$
308/338 m	$0.003 \leq \xi \leq 0.024$	$0.003 \leq \xi \leq 0.022$
420 m	$0.002 \leq \xi \leq 0.016$	$0.002 \leq \xi \leq 0.013$

In this Section, for each resolution effect one detector location was chosen as an example. A simple argument of the size of the effect is given for that location and simulated results are presented. In Figs. 7.5–7.9, the distribution and profile plots include the error due to the method. In Figs 7.10–7.12, the error due to the method is subtracted quadratically.

7.2.1 Detector resolution

The 10 μm detector resolution can change the difference $(x_{430} - x_{420})$ by 20 μm. According to the $(x_{430} - x_{420})$ vs. x_{420} plot, a 10 μm change in the mean coordinate and a 20 μm change in the difference of coordinates may change ξ by 0.0002 for ξ=0.0025 and by 0.0001 for ξ=0.014. Thus the estimate for the relative error is 8% for ξ=0.0025 and 0.7% for ξ=0.014.

The effect of the 10 μm detector resolution for reconstructing ξ at the 420 m location is shown in Fig. 7.5. The relative deviation depends on ξ and it is larger for small ξ values. For ξ=0.002 the relative deviation is about 0.07 and if ξ=0.015 it is a few per mille. The simulated values are consistent with the estimated ones.

7.2.2 Beam position

The width of the distribution for $|\xi_{\max} - \xi_{\min}| = 5 \cdot 10^{-4}$ m at x_{308} vs. x_{338} plot is $2.74 \cdot 10^{-4}$ m for ξ=0.006 and $1.5 \cdot 10^{-4}$ m for ξ=0.0155. A 5 μm beam position resolution corresponds to a 0.02 and a 0.033 relative change in the widths of distributions for ξ=0.006 and ξ=0.0155, respectively. The same relative change corresponds to a 10^{-5} and an $1.7 \cdot 10^{-5}$ absolute change in the ξ values. Thus the estimate for the relative deviation due to the 5 μm beam position resolution is $10^{-5}/0.006 \approx 0.0017$ for ξ=0.006 and $1.7 \cdot 10^{-5}/0.0155 \approx 0.0011$ for ξ=0.0155.

The relative deviation due to the 5 μm beam position resolution at the 308 m location is shown in Fig. 7.6. The deviation at the 308 m location is independent of ξ and the effect of the 5 μm beam position resolution is roughly 0.4%. The simulated effect of 5 μm beam position resolution
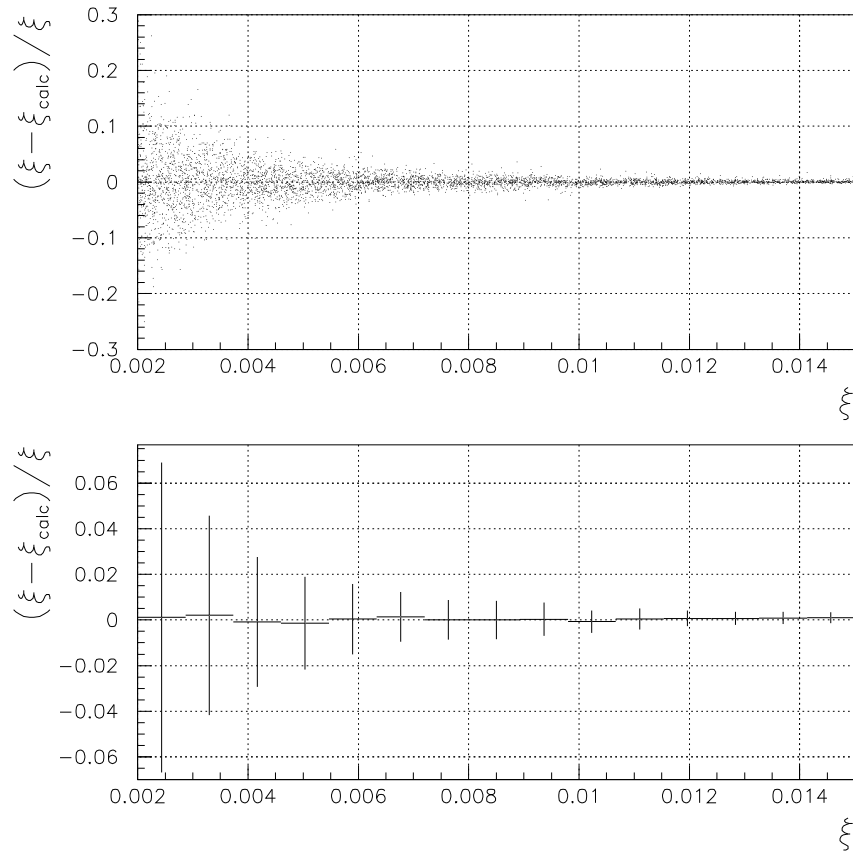
Figure 7.5: Relative deviation of the ξ reconstruction due to a 10 μm detector resolution at the 420 m location. The lower plot indicates the central value and the rms of the upper one.

includes also the error due to the method itself. Thus the simulated and estimated sizes and shapes of the errors are consistent with each other.

7.2.3 Transverse beam size

In the accelerator the particles travel in bunches, whose projection in the (x, y)-plane is an ellipsoid. Thus the particles do not always collide exactly in the origin of the reference frame.

The magnification at 308 m is about 6 and at 338 m it is about 12. Using Eq. (3.15), the 16 μm transverse beam size at the IP changes x_{308} coordinate by 112 μm and x_{338} coordinate by 240 μm. In the x_{308} vs. x_{338} plot such a change in the coordinates will induce a 0.0002 change in ξ values for both ξ=0.005 and ξ=0.015. Then the estimate for the relative error is 4% and 1.3% for ξ=0.005 and ξ=0.015, respectively.

As an example, the effect of the 16 μm transverse beam size at the 308 m location can be seen in Fig. 7.7. The spread decreases with increasing ξ. For ξ=0.005 it is about 4% and for ξ=0.025 it is about 1.5%. The transverse beam size is one of the dominating effects of the ones which have been studied. The simulated and estimated sizes and shapes of the errors are mutually consistent.

7.2.4 Beam divergence

The beam divergence only changes θ_x^*. Since the ξ reconstruction is independent of θ_x^* value, the effect of beam divergence should be negligible.

The effect of the 30 μrad beam divergence at the 215 m location is shown in Fig. 7.8. The relative deviation is independent of ξ and its magnitude is about 0.1%. Since the deviation includes also the error due to the method itself, the effect of beam divergence on the ξ reconstruction is negligible.

7.2.5 Beam energy spread

There is an uncertainty in the beam energy which causes uncertainty in the ξ. Let us assume that the beam energy is changed from E_B to $(1 - \delta)E_B$. Then the relative error of ξ changes as

$$\frac{\xi_{\text{changed}} - \xi}{\xi} = \frac{\frac{(1+\delta)E_B - E_p}{(1+\delta)E_B} - \frac{E_B - E_p}{E_B}}{\frac{E_B - E_p}{E_B}} = \frac{\delta}{1+\delta}\left(\frac{1-\xi}{\xi}\right) \approx \frac{\delta}{\xi}, \qquad (7.1)$$

where E_p is the energy of the leading proton and the last approximation is valid since $\delta \ll 1$ and $\xi \ll 1$. Then the calculated relative error due to a 10^{-4} energy spread for ξ=0.003 is 3.3% and for ξ=0.014 is 0.7%.

Figure 7.9 shows the relative error at the 420 m location due to the energy spread of 10^{-4}. The relative deviation is a decreasing function of ξ
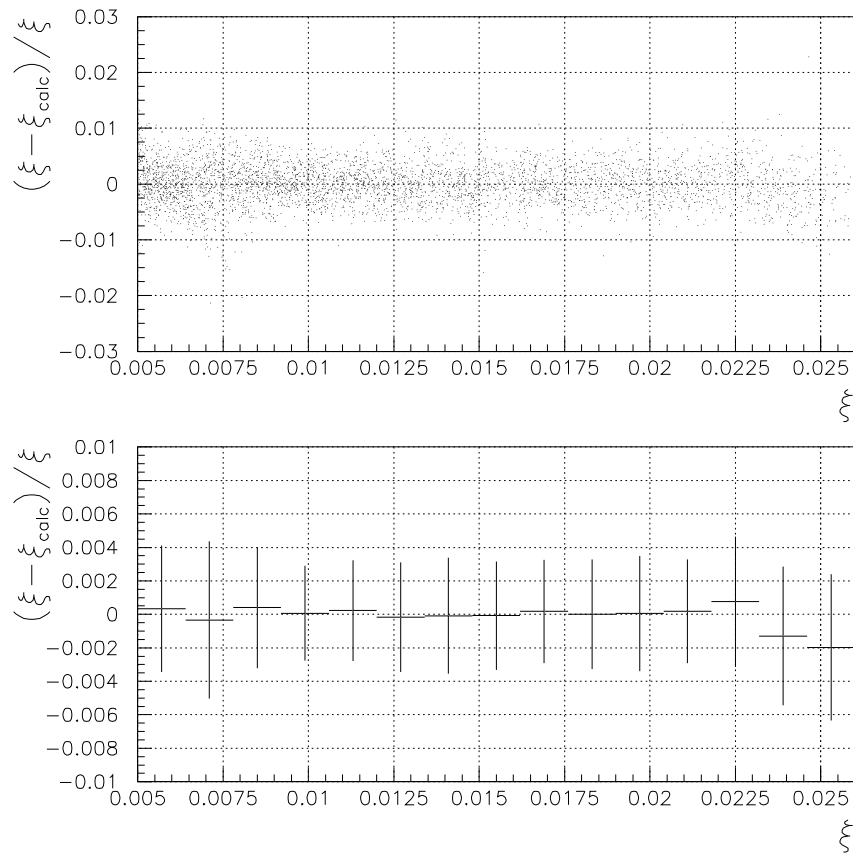
Figure 7.6: Relative deviation of the ξ reconstruction due to a 5 μm beam position resolution at the 308 m location. The lower plot indicates the central value and the rms of the upper one.

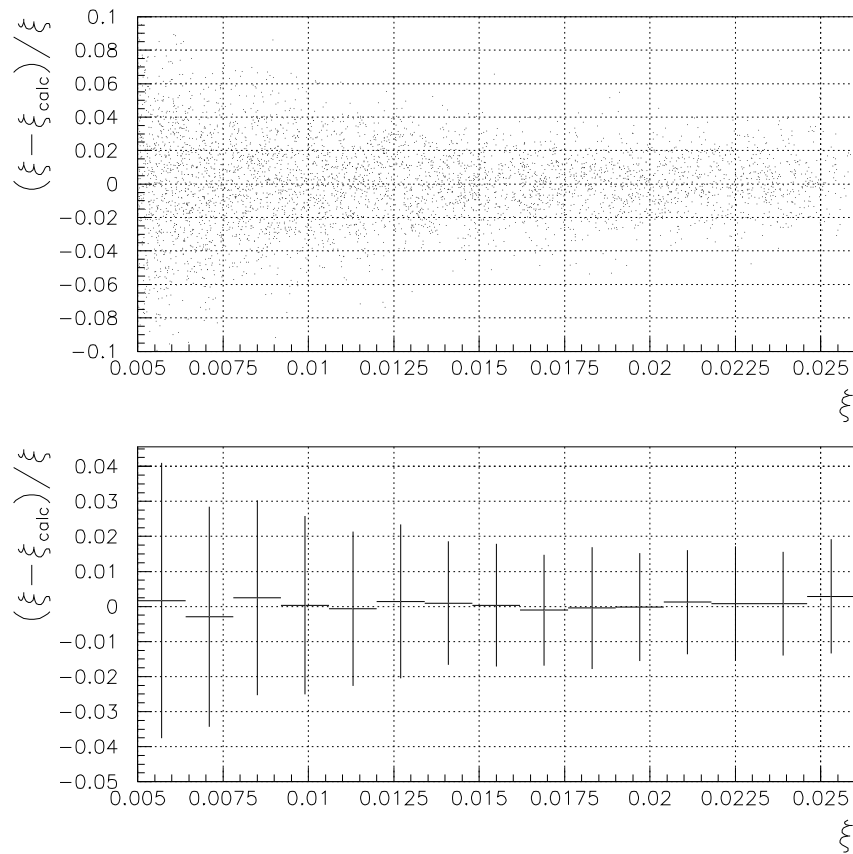Figure 7.7: Relative deviation of the ξ reconstruction due to a 16 μm transverse beam size at the 308 m location. The lower plot indicates the central value and the rms of the upper one.
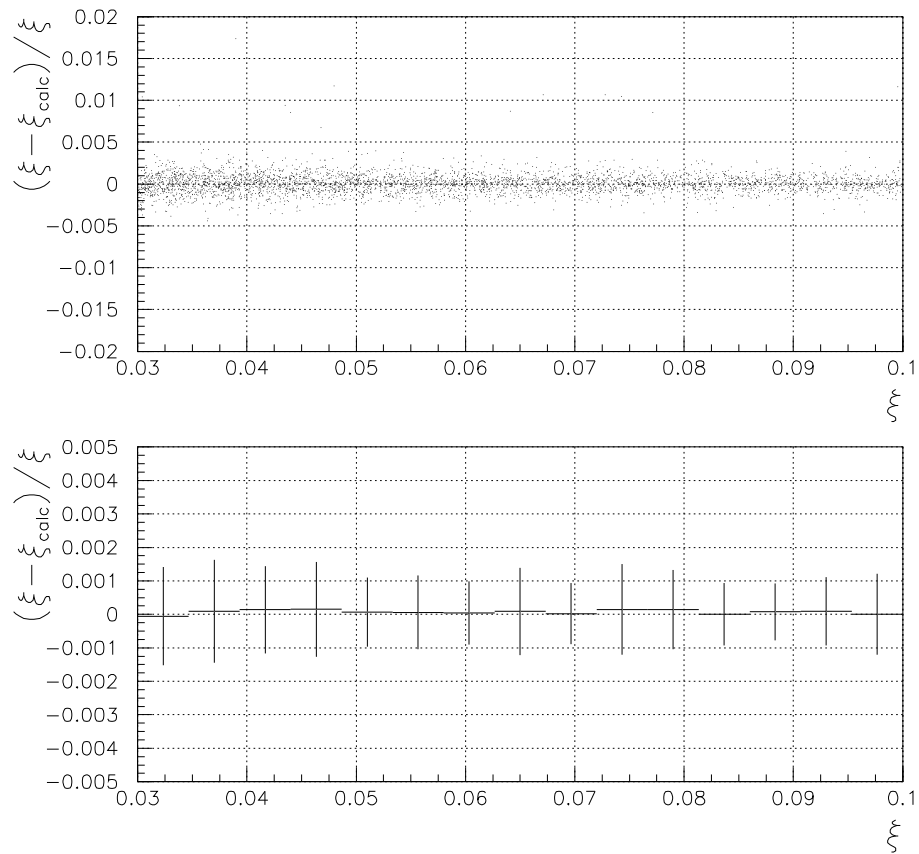
Figure 7.8: Relative deviation of the ξ reconstruction due to a 30 μrad beam divergence at the 215 m location. The lower plot indicates the central value and the rms of the upper one.

and it is about 3% for ξ=0.003 and less than 1% for ξ=0.014. The size and shape of the simulated effect correspond the calculated ones.

7.2.6 Total resolution

All the resolution effects studied are combined in Figs. 7.10, 7.11 and 7.12 for the 215 m, 308 m and 420 m locations, respectively. In the figures, open blue triangles correspond to a 10 μm detector resolution, filled green circles correspond to a 5 μm beam position resolution, filled red squares correspond to a 16 μm transverse beam size, open blue squares correspond to a 30 μrad beam divergence and filled pink triangles correspond to a 10^{-4} energy spread. Blue filled circles mark the relative deviation when all the resolution effects studied are taken into account in simulations. Open black crosses are calculated effect due to all separate resolution effects, i.e.

$$\sigma_{\text{calc}} = \sqrt{\sigma_1^2 + \sigma_2^2 + \sigma_2^2 + \sigma_3^2 + \sigma_4^2 + \sigma_5^2}, \qquad (7.2)$$

where σ_n are deviations of detector resolution, beam position resolution, transverse beam size, beam divergence and energy spread.

The most dominant resolution effects at the 215 m location are the transverse beam size and detector resolution. The deviation due to the transverse beam size decreases from 1.6% to 0.5% for ξ values from 0.03 to 0.1 and the deviation due to detector resolution fluctuates between 1–1.5%. The deviations due to beam position smearing, beam divergence and energy spread are negligible compared to the aforementioned ones.The total resolution due to all five resolution effect decreases from 2% to 1%.

At the 308 m location, the transverse beam size is the most dominant effect. The resolution due to it decreases from 3.5% to 1.5% for clockwise moving protons ($0.005 < \xi < 0.026$) and from 4% to 2% for anticlockwise moving protons ($0.005 < \xi < 0.022$). The second largest resolution is the energy spread for small ξ values and the detector resolution for large ξ values. The magnitudes of the second largest resolutions are 1.7% for small ξ values and 1.2% for large ξ values. The resolutions due to beam position resolution and beam divergence are small compared to the other three. The total resolution decreases from 4% to 2–2.5% on the ξ values from 0.005 to 0.026.

Also at the 420 m location the transverse beam size is the most dominant effect. For ξ=0.003 the deviation due to the transverse beam size is 7% and for ξ=0.015 it is few per mille for clockwise moving protons and the corresponding resolutions for anticlockwise moving protons are 12% and few per mille. For small ξ the second and third largest deviations are caused by detector resolution and energy spread. For large ξ all the deviations are less than 1%. The total deviation for clockwise moving protons is about 10% for ξ=0.003 and few per mille for ξ=0.014. The corresponding numbers for anticlockwise moving protons are 15% and few per mille.
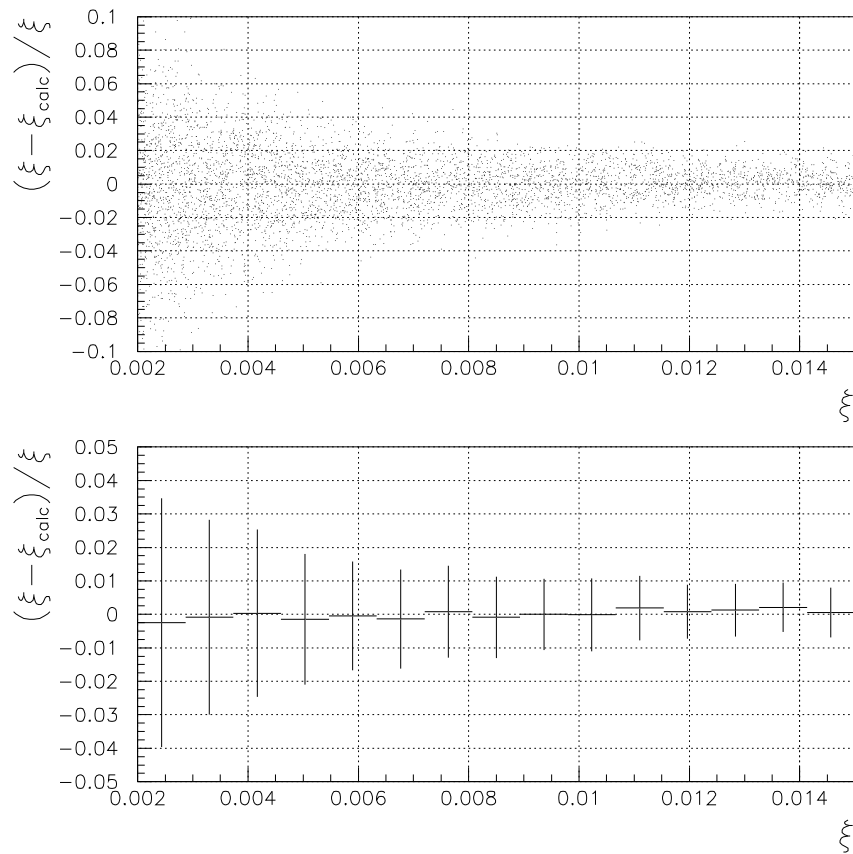
Figure 7.9: Relative deviation of the ξ reconstruction due to a 10^{-4} energy spread at the 420 m location. The lower plot indicates the central value and the rms of the upper one.
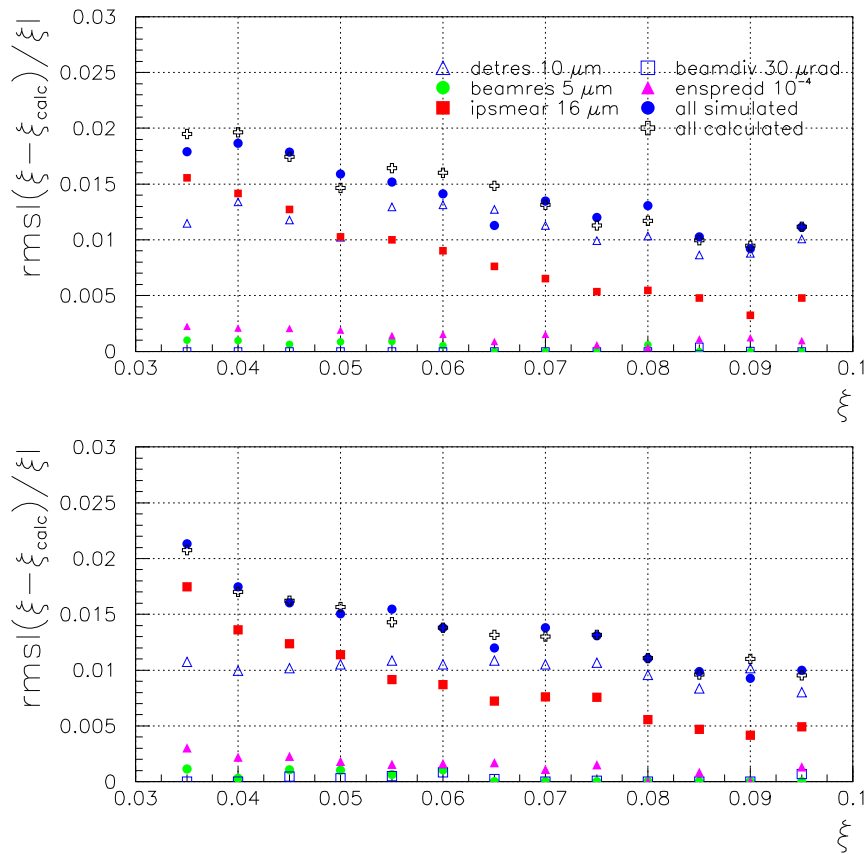
Figure 7.10: Summary of all the studied resolution effects at the 215 m location. The upper plot is for clockwise moving protons and the lower one for anticlockwise moving protons.
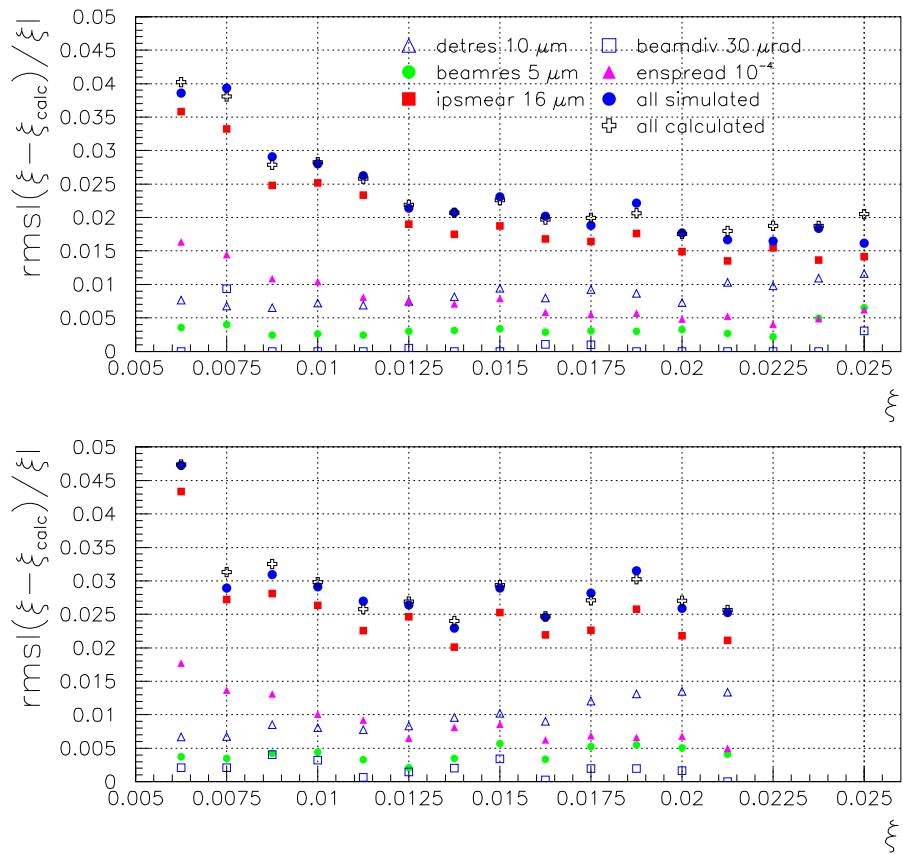
Figure 7.11: Summary of the all studied resolution effects at the 308 m location. The upper plot is for clockwise moving protons and the lower one for anticlockwise moving protons.
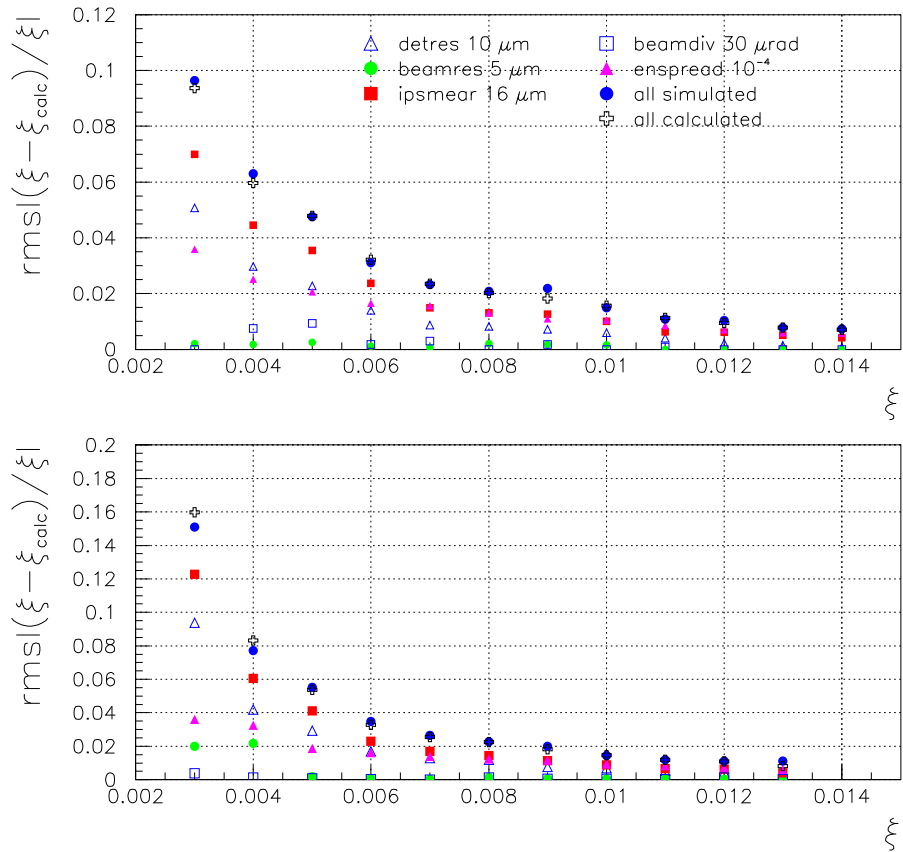
Figure 7.12: Summary of all the studied resolution effects at the 420 m location. The upper plot is for clockwise moving protons and the lower one for anticlockwise moving protons.

7.3 Systematic shifts

The systematic shifts on the measured coordinates at the detector location were studied in a way similar to the resolution effects.

7.3.1 Beam position

A beam position offset does not change the value of $(x_{225} - x_{215}) \sim \theta_{x,215}$, only x_{215} is changed by e.g. 10 μm. In the $(x_{225} - x_{215})$ vs. x_{215} plot, a 10 μm change in x_{215} coordinate corresponds to a 0.0001 change in the ξ values for both ξ=0.03 and ξ=0.1. Thus the estimated magnitude of the shift in the relative error is 0.3% for ξ=0.03 and 0.1% for ξ=0.1.

The effect of a 10 μm systematic shift of the absolute beam position at the 215 m location is shown in Fig. 7.13. The average of relative error is negative and the absolute value of the relative error decreases as a function of ξ. For ξ=0.03 the average of the relative error is –0.3% and for ξ=0.1 it is about –0.1%.

7.3.2 Detector misalignment

Since the other measured coordinate at the 420 m location is $\theta_x \sim (x_{430} - x_{420})$, the estimate for the error can be easily calculated with Fig. 6.1. For ξ=0.002 the difference $(x_{430} - x_{420})$ is about $5 \cdot 10^{-4}$ m. A 10 μm systematic shift correspond to a 2% shift in the angle and can be straightforwardly approximated to be a 2% shift in the average of the relative error. For ξ=0.015 the estimate for systematic shift in the relative error is 0.25%.

The effect of a –10 μm systematic shift due to the detector misalignment for the 420 m location is shown in Fig. 7.14. The average of the relative error is negative and its magnitude strongly depends on ξ. For ξ=0.002 the shift of the relative error is about –4% and for ξ=0.015 it is few per mille. The simulated size and shape of the shift in the relative error are consistent with the estimated ones.

7.3.3 Comparison of the two systematic shifts

All the systematic shifts studied are combined in Figs. 7.15, 7.16 and 7.17 for the detector locations at 215 m, 308 m and 420 m, respectively. Filled pink triangles mark the average of relative shift for beam position offset and open red circles mark the average of relative shift for detector alignment.

Detector misalignment is the dominant effect of the two systematic shifts at the 215 m location. In the detector misalignment only the coordinates the measured at the second station are shifted. Since the values of measured coordinates at the 215 m location are order of 10^{-3} m and the difference between two measured coordinates are order of 10^{-4} m, the relative change of 10 μm is larger for the difference of coordinates. The average of relative
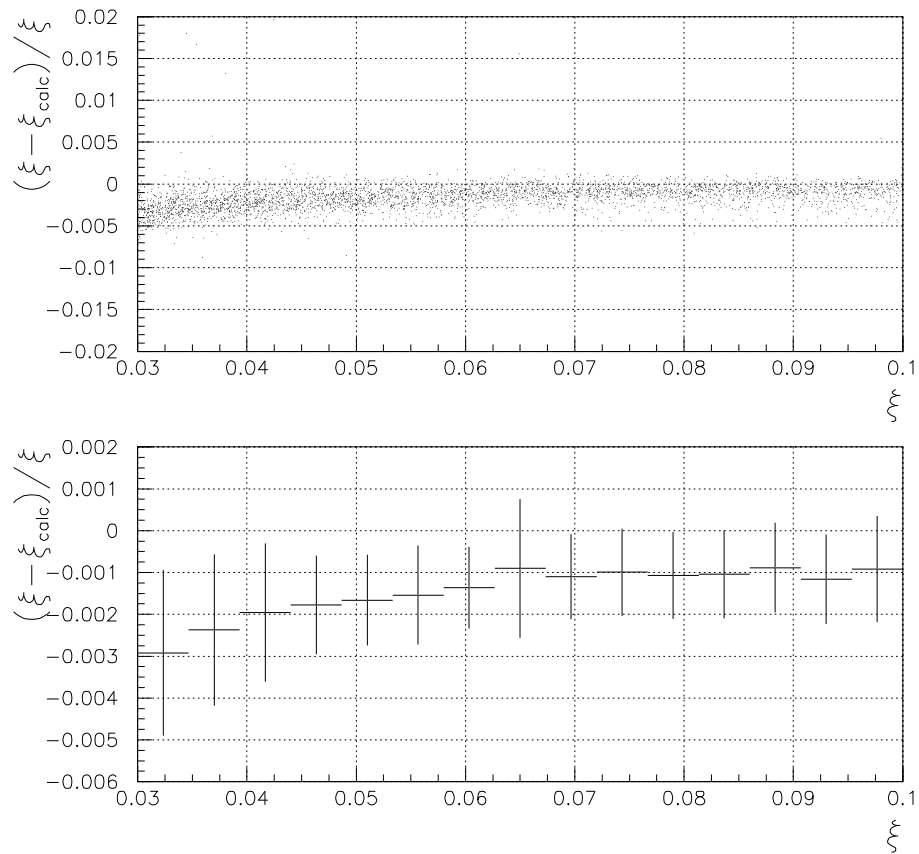
Figure 7.13: Relative error of the ξ reconstruction due to a 10 μm beam offset at the 215 m location. The lower plot indicates the central value and the rms of the upper one.
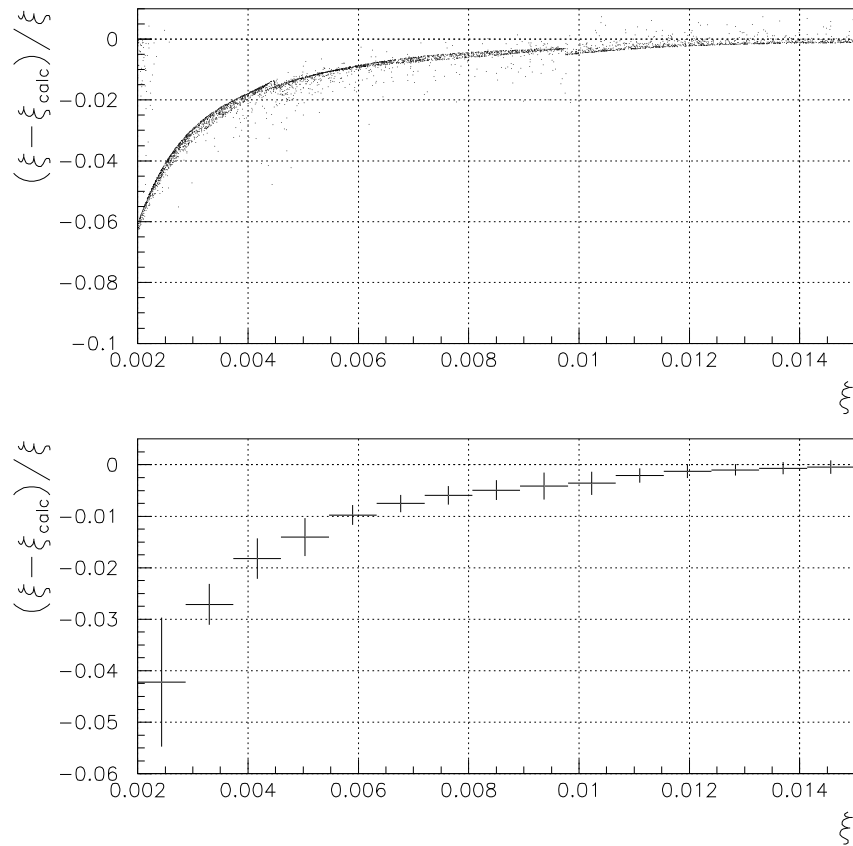
Figure 7.14: Relative error of the ξ reconstruction due to a $-10\ \mu$m detector alignment at the 420 m location. The lower plot indicates the central value and the rms of the upper one.

error due to a –10 μm detector misalignment is negative and the magnitude is about 0.6–0.8%. The magnitude of relative shift due to detector misalignment is roughly the same as the total resolution for ξ=0.1 and it is about 1/2 for ξ=0.03.

At the 308 m location, the beam position offset is the leading systematic shift and the average of relative error due to it increases from 0.6% to 0.8% in the range of acceptance. For ξ=0.005 the fraction of the systematic shift to the total resolution is about 1/4 and for ξ=0.025 it is about 1/2.

Because of the same reason as for the 215 m location, the detector misalignment is the dominant systematic shift at the 420 m location. For clockwise moving protons, the average of the relative error due to a –10 μm detector misalignment is about –3.5% for ξ=0.003 and minus few per mille for ξ=0.014. The corresponding numbers for anticlockwise moving protons are about 7% and minus few per mille. The magnitude of the relative shift is about 2/5 of the total resolution for ξ=0.003 and it is about 1/3 for ξ=0.01.

A procedure for performing the detector alignment and minimization of the systematic beam position shift needs to be developed.

7.4 Mass resolution

The reconstructed mass of the central system can be calculated with the missing mass method, see formula (2.25), from the reconstructed ξ values. The calculated ξ values were chosen in such a way that if the ξ value of the event is in the acceptance of the 420 m detector, ξ_{calc} was calculated with the 420 m method from the measured coordinates at the 420 m location. The 308 m location was used for ξ_{calc} if the simulated ξ was in the acceptance of the 308 m location but not in the acceptance of the 420 m location. Finally, the measurement at the 215 m location was used for events which cannot be detected at the 420 m and 308 m detector locations.

The relative error

$$\frac{M - M_{\text{calc}}}{M} \tag{7.3}$$

due to the ξ reconstruction methods is shown in the upper plot in Fig. 7.18. The relative spread is independent of mass M and the magnitude of the relative error is about 0.1%. The mean value of the distribution is 0. Thus the mass reconstruction works with high accuracy. The effect of all the five resolution effects is shown in the lower plot in Fig. 7.18. The spread decreases for increasing M and it is about 3.5% for small masses and about 1.5% for M=800 GeV.

In contrast to the previous plots, the mass resolution for each bin was calculated using a Gaussian fit instead of RMS. It is shown in Fig. 7.19. Filled black circles mark the resolution when all detectors exist. Calculated ξ values were chosen as described above. Open red squares correspond to
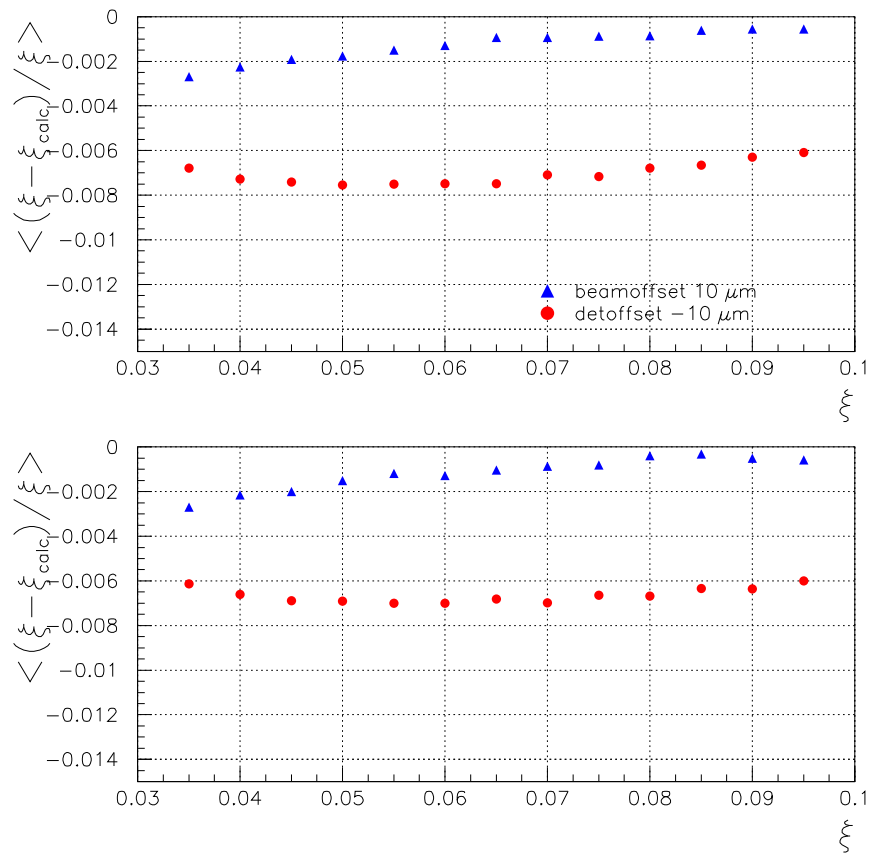
Figure 7.15: Summary of all the studied offsets at the 215 m location. The upper plot is for clockwise moving protons and the lower one for anticlockwise moving protons.
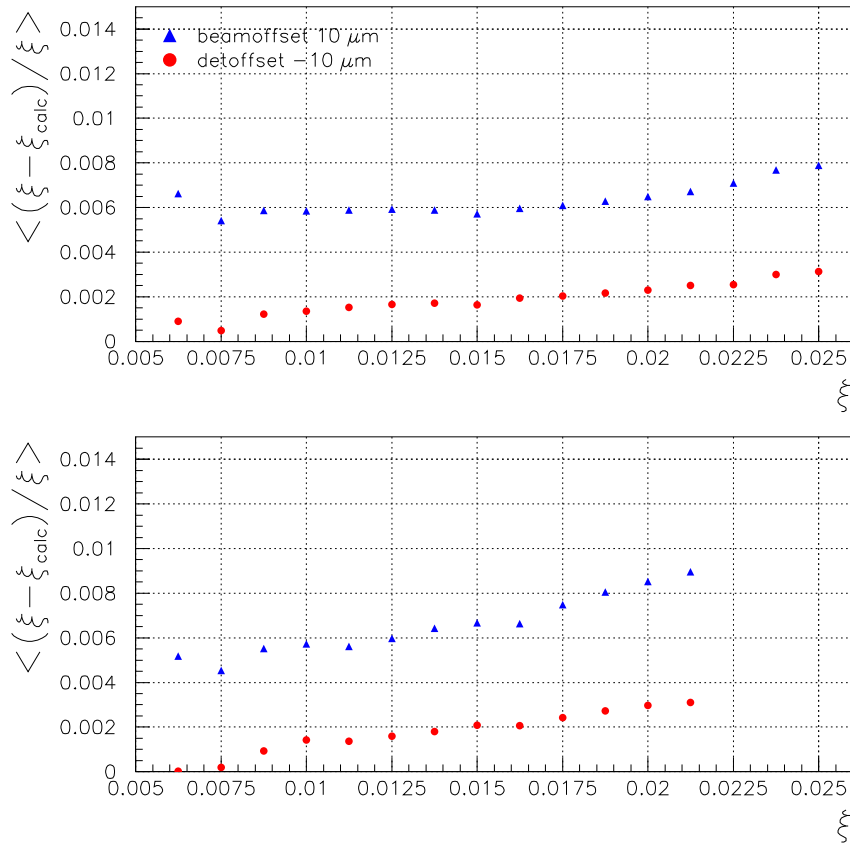
Figure 7.16: Summary of all the studied offsets at the 308 m location. The upper plot is for clockwise moving protons and the lower one for anticlockwise moving protons.
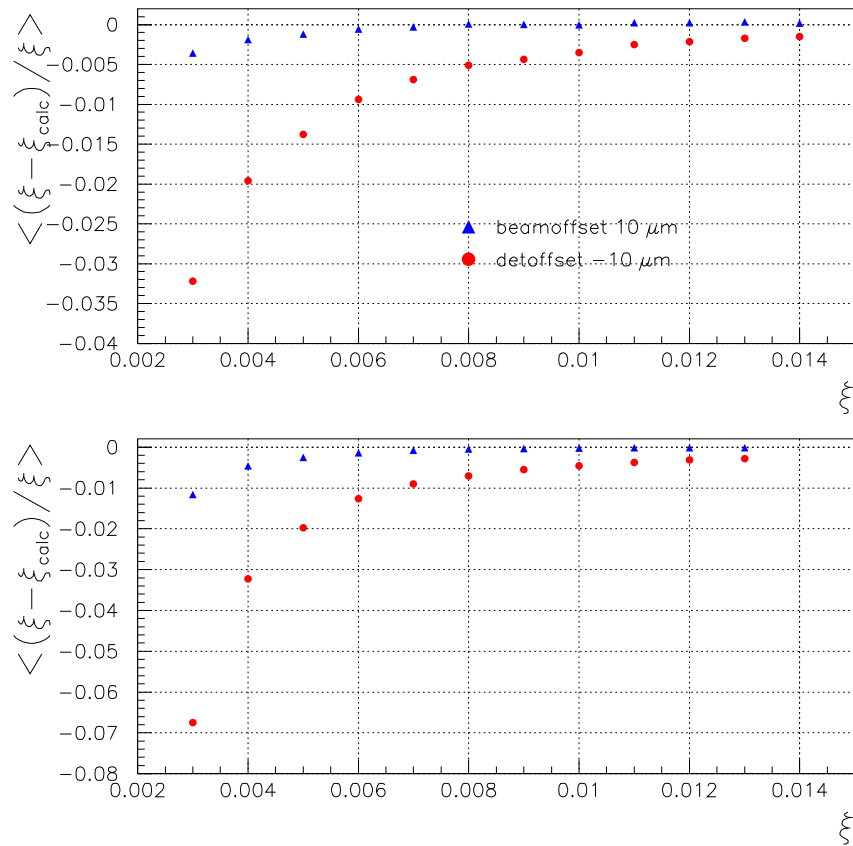
Figure 7.17: Summary of all the studied offsets at the 420 m location. The upper plot is for clockwise moving protons and the lower one for anticlockwise moving protons.

the total mass resolution for the 215 m location alone, filled green triangles correspond to the total mass resolution for the 308 m location alone and open blue crosses mark the total mass resolution for the 420 m location alone.

For large masses $M \geq 500$ GeV, the total mass resolution is the same for all detector locations and the 215 m location alone. For small masses the best mass resolution is achieved with the 308 m location alone for $M \leq 110$ GeV and with the 420 m location alone for $M \geq 110$ GeV. However, the masses $M \leq 60$ GeV cannot be detected at the 308 m location alone and the masses $M \geq 200$ GeV cannot be detected at the 420 m location alone.

The mass resolution decreases for increasing mass. With all detector locations the mass resolution is about 4% for $M=60$ GeV, 2% for $M=120$ GeV and 1% for $M \geq 400$ GeV. The mass reconstruction is more accurate with only one detector location for small masses, but the acceptance is less if only one detector location exists. The mass acceptance for small masses is shown in Fig. 7.20. In a case when the proton is seen in more than one station, the mass acceptance may be improved further by properly combining the measurements.

The reconstruction methods used in this thesis do not cover the whole ξ acceptance at all detector locations. At the 215 m location the ξ value was reconstructed for protons with $\xi \geq 0.03$. At the 308 m location the lowest reconstructed ξ value was 0.005. Otherwise the ξ values were reconstructed in the range of acceptance at each detector location. The mass acceptance according to the reconstruction methods used is shown in Fig. 7.21.
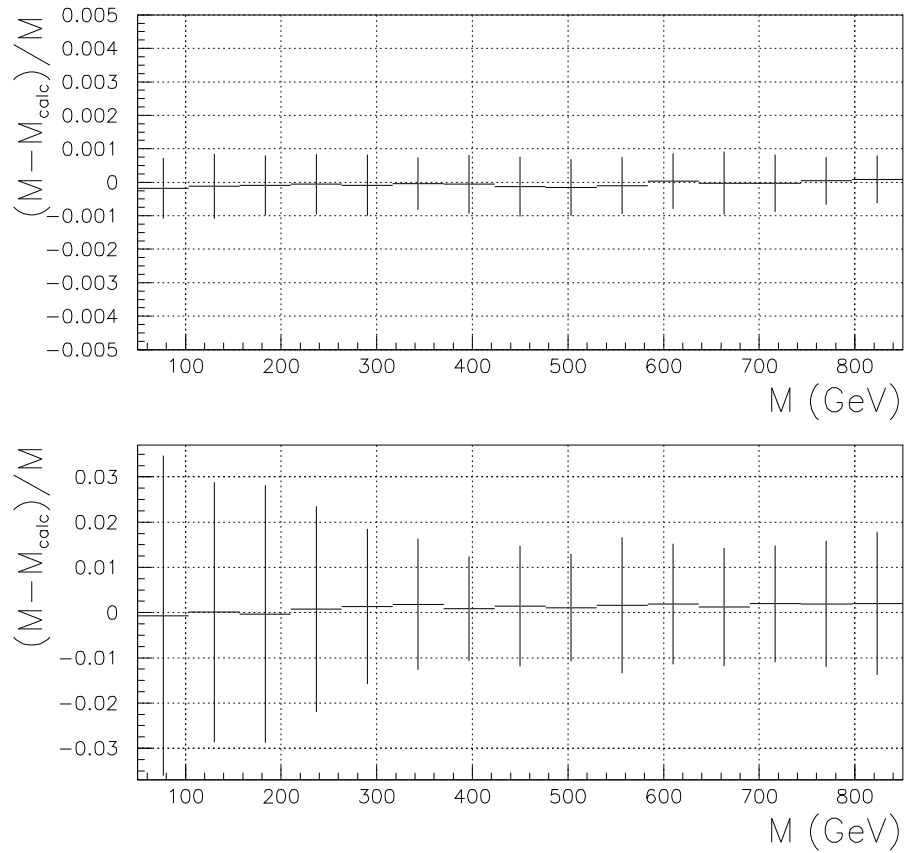
Figure 7.18: Mass reconstruction accuracy due to the ξ reconstruction method in the upper plot and expected mass resolution in the lower plot.
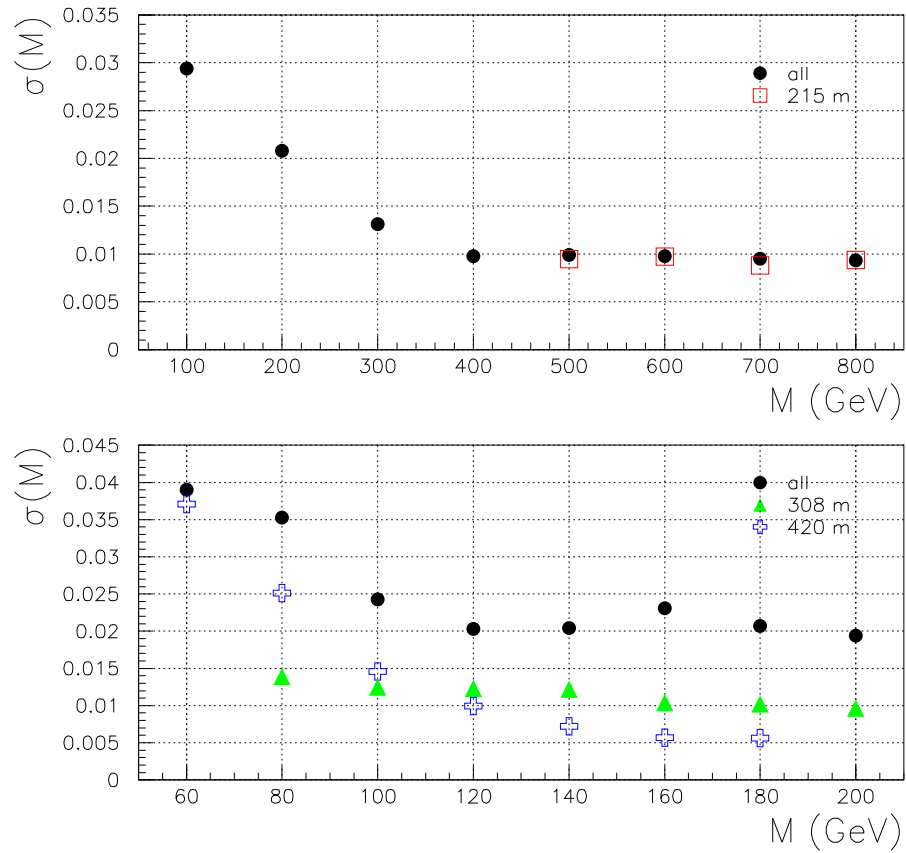
Figure 7.19: Combined mass resolution of all detector locations and mass resolution for each location separately.
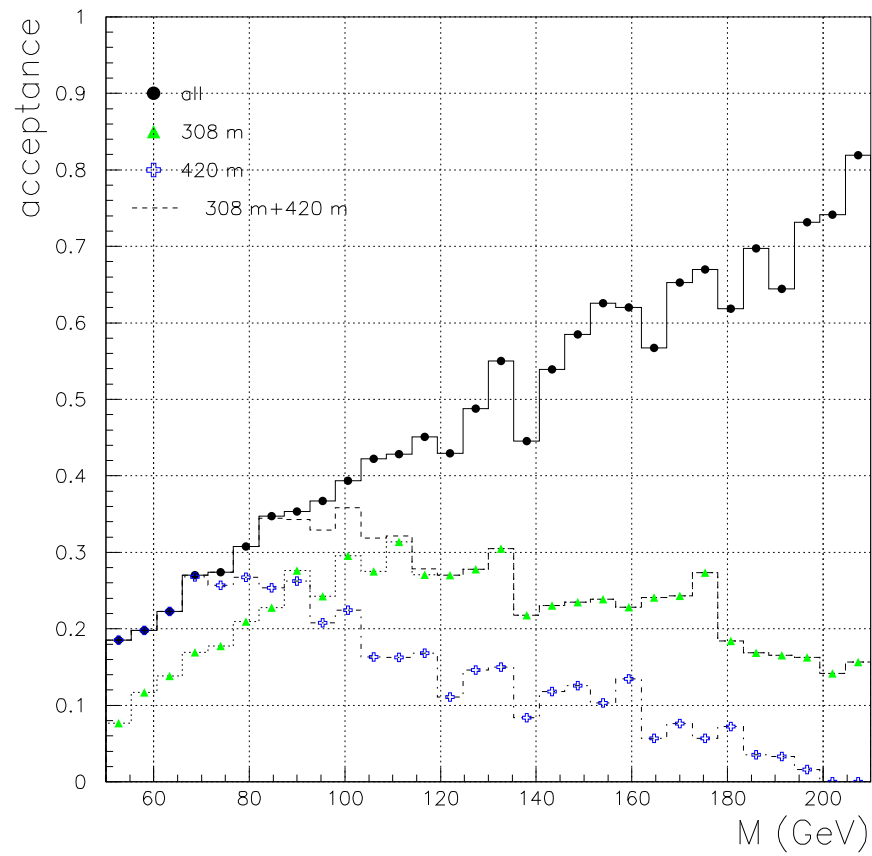
Figure 7.20: Mass acceptance for small masses.
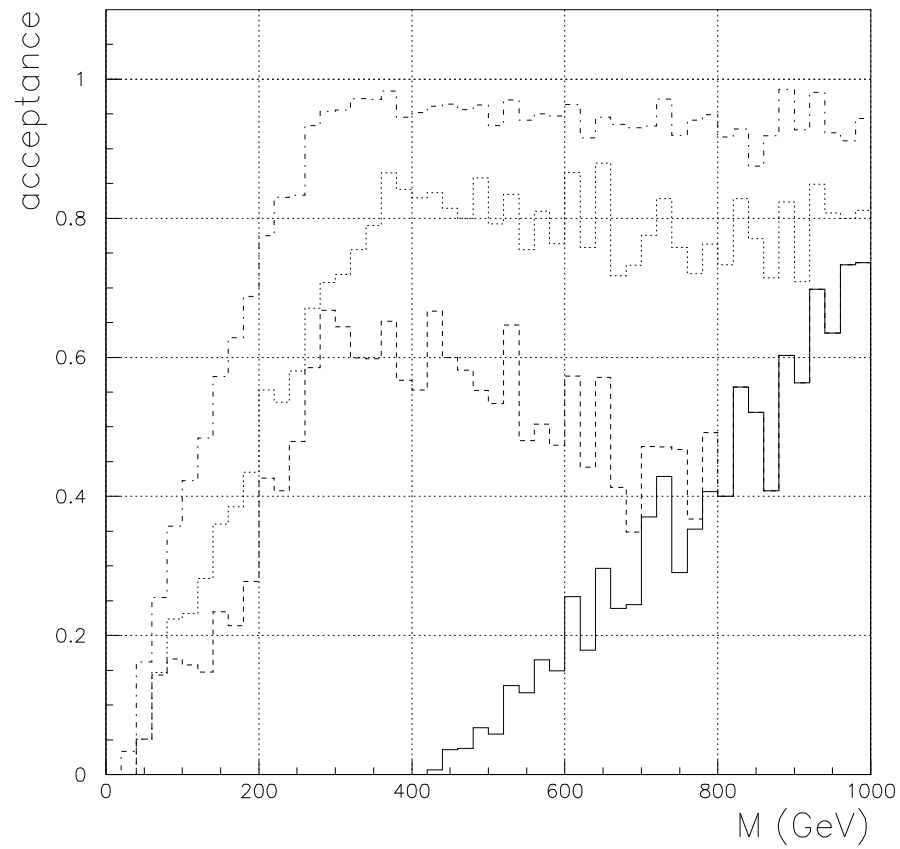
Figure 7.21: Mass acceptance according to the available reconstruction methods. The solid line is the mass acceptance of the reconstruction methods at the 215 m locations, the dashed line is the combined mass acceptance of the reconstruction methods at the 215 m and 420 m locations and the dotted line is the combined mass acceptance of all the reconstruction methods. The dashed-dotted line corresponds to ideal acceptance of all the stations.

Chapter 8

Conclusions

The aim of this thesis was to study the mass resolution of the central system in exclusive double Pomeron exchange ($pp \rightarrow p + X + p$) via the leading proton measurement. This centrally produced X could be the Higgs boson, and it has been proposed that via leading proton measurement, the mass can be measured to an accuracy of $\mathcal{O}(1 \text{ GeV})$ per event, whereas the direct measurement of the Higgs mass via its decay products in $H \rightarrow b\bar{b}$ results in a mass resolution of only about $\mathcal{O}(10 \text{ GeV})$ per event.

The trajectories of the leading protons have to be detected far away from the interaction point. We selected the detector locations to be at 215 m, 308 m and 420 m from the interaction point. At the 215 m and 420 m locations, the measured coordinates were the x displacement and the polar angle component θ_x. At the 308 m location the two measurements were the x displacements at 308 m and 338 m from the interaction point.

The ξ acceptance was covered between ξ=0.002–0.1 with these three detector locations. The difference in the combined mass acceptance of all the three detector locations compared to the combined mass acceptance of the 215 m and 420 m detector locations together was about 10% for the central system of mass M_X=120 GeV. The masses measured with better than 50% acceptance, were 140 GeV for the combined mass acceptance of all three detector locations, 170 GeV for combined mass acceptance of the 215 m and 420 m locations, and 620 GeV for the 215 m location alone.

The accuracy of the momentum reconstruction suffers from different resolution effects and systematic shifts. The resolution effects studied were detector resolution (10 μm), beam position resolution (5 μm), transverse beam size (16 μm), beam divergence (30 μrad) and energy spread (10^{-4}). The transverse beam size had the dominant effect on reconstruction accuracy and, at the 215 m and 420 m locations, the detector resolution also had a significant effect, as well as the energy spread for smallest ξ values. The beam position resolution and beam divergence had negligible effect on reconstruction accuracy compared to the aforementioned ones. The total

resolution due to all the resolution effects studied decreased for increasing ξ. For example, the total resolution was about 10% for ξ=0.002, 2% for ξ=0.02 and 1% for ξ=0.1.

The systematic shifts studied were detector offset (-10 μm) and beam position offset (10 μm). At the 215 m and 420 m locations, the detector offset caused a larger shift in the reconstructed values and at the 308 m location, the beam position offset was the dominant one. For the largest ξ values at the 215 m location the relative shift and the total resolution were both about 1%. For smaller ξ values the relative shift in reconstruction is about 1/4–1/2 of the magnitude of total resolution.

The mass resolution was studied using the missing mass method to calculate the reconstructed mass from the calculated ξ values. The total mass resolution decreases with increasing mass. With all detector locations the mass resolution is about 4% for M=60 GeV, 2% for M=120 GeV and 1% for $M \geq 400$ GeV. The mass resolution at small masses can be improved when only one detector location is chosen. However, the acceptance decreases if only one detector location is used.

In the future, the more realistic aperture of the beam pipe should be implemented. However, it will only affect the ξ acceptance for largest ξ values. The ξ reconstruction methods have to be refined to cover the full ξ range, and one could use a two-dimensional grid with linear interpolation for ξ reconstruction at all detector locations and compare results.

The inaccuracy in the alignment of the magnetic elements and the variations of magnetic field strength with respect to nominal values will affect in ξ reconstruction and thus they should be studied. It may also be worth studying reconstruction of θ_x^* and θ_y^*, and how the inaccuracies affect $\theta_{x,y}^*$ reconstructions.

This study was performed with the LHC optics. The LHC is planned to be ready in 2007, and it should be able to detect the Higgs boson and supersymmetric particles, if they exist. Double Pomeron exchange via leading proton measurement provides a clean signature for finding them.

Bibliography

[1] B. R. Martin and G. Shaw, Particle Physics, Second ed. John Wiley & Sons (1997).

[2] Particle Data Group, Review of Particle Physics, Physical Review **D 66**, (2002).

[3] F. Halzen and A. D. Martin, Quarks & Leptons: An Introductory Course in Modern Particle Physics, John Wiley & Sons (1984).

[4] M. L. Good and W. D. Walker, Diffraction Dissociation of Beam Particles, Phys. Rev. **120**, 1857 (1960).

[5] K. Goulianos, Diffraction in hadron-hadron interactions, hep-ex/0011060 (2000).

[6] K. Goulianos, Results on Diffraction, hep-ex/9708004 (1997).

[7] P. D. B. Collins and A. D. Martin, Hadron Interactions, Adam Hilger Ltd (1984).

[8] K. Goulianos, Diffractive interactions of hadrons at high energies, Phys. Reports, **101**, 171 (1983).

[9] A. Donnachie and P. V. Landshoff, Total Cross Sections, hep-ph/9209205 (1992).

[10] A. De Roeck, V. A. Khoze, A. D. Martin, R. Orava and M. G. Ryskin, Ways to detect a light Higgs boson at the LHC, hep-ph/0207042 (2002).

[11] V. A. Khoze, A. D. Martin and M. G. Ryskin, Diffractive Higgs Production:Myths and Reality, hep-ph/0207313 (2002).

[12] The LHC Study Group, The Large Hadron Collider Conceptual Design, CERN/AC 95-05 (1995).

[13] H. Wiedemann, Particle Accelerator Physics: Basic Principles and Linear Beam Dynamics, Springer-Verlag (1993).

[14] FELIX Collaboration, FELIX Letter of Intent, CERN/LHCC 97-45 (1997).

[15] TOTEM Collaboration, TOTEM-Technical Proposal, CERN/LHCC 99-7 (1999).

[16] CMS Collaboration, CMS-Technical Proposal, CERN/LHCC 94-38 (1994).

[17] CMS Collaboration, The Trigger Systems - Technical Design Report, Volume 1, CERN/LHCC 2000-38 (2000).

[18] V. P. Nomokorov, The Microstation Concept for Forward Physics, published in Forward Physics and Luminosity Determination at LHC, K. Huitu, V. Khoze, R. Orava and S. Tapprogge (2000).

[19] A. De Roeck, Panel Discussion on Forward Physics Measurements at the LCH Experiments, published in Forward Physics and Luminosity Determination at LHC, K. Huitu, V. Khoze, R. Orava and S. Tapprogge (2000).

[20] R. Engel, Phys. Rev. D **51** 3220 (1995).

[21] A. Capella, U. Sukhatme, C. I. Tan and J. Tran Thanh Van, Phys. Rep. **236** 227 (1994).

[22] T. Sjöstrand, Computer Physics Commun. **94**, 74 (1994).

[23] Personal discussions with Jerry Lämsä at CERN.

[24] F. C. Icelin, J. M. Jowett, J. Pancin and A. Adelmann, MAD 9 Version 9, CERN-SL-2000-026 AP (2000).

[25] http://lhc-new-homepage.web.cern.ch/lhc-new-homepage/

[26] T. Mäki, Special assignment: The performance of reconstructing the Higgs boson mass in exclusive process at LHC, Helsinki University of Technology (2002).

[27] J. Kalliopuska, Special assignment: The method for reconstructing the Higgs boson mass in exclusive process at LHC, Helsinki University of Technology (2003).

[28] N. Marola, Special assignment: Studies of the leading proton momentum reconstruction and the Higgs mass resolution in diffractive Higgs production at the LHC, Helsinki University of Technology (2002).

Appendix A

Parameters of momentum reconstruction

The parameters for momentum reconstruction methods are given here. Table A.1 contains the constants c_n from surface 6.2 for clockwise moving protons and Table A.2 contains the constants c_n for anticlockwise moving protons. The parameters a_n for surface 6.4 are given in Tables A.3 and A.4 for clockwise and anticlockwise moving protons, respectively.

Table A.1: Surface constants for the fitted surface at 308 m for clockwise moving protons.

	c_1	c_2	c_3	c_4	c_5	c_6
$0.005 \leq \xi \leq 0.015$	-0.245	-0.213	-0.245	-0.229	-119.5	-0.000207
$0.015 \leq \xi \leq 0.026$	-1.332	-0.216	-1.325	-0.231	-167.7	-0.000360

Table A.2: Surface constants for the fitted surface at 308 m for anticlockwise moving protons.

	c_1	c_2	c_3	c_4	c_5	c_6
$0.005 \leq \xi \leq 0.015$	-1.145	-0.159	-1.145	-0.172	-180.3	0.000563
$0.015 \leq \xi \leq 0.022$	-5.747	-0.0404	-5.732	-0.0608	-242.7	0.0132

Table A.3: Surface constants for the fitted surface at 420 m for clockwise moving protons.

y'	a_1 a_6	a_2 a_7	a_3 a_8	a_4 a_9	a_5 a_{10}
$[-60, -30]$	$-1.31 \cdot 10^{-5}$ $4.38 \cdot 10^{-7}$	$2.13 \cdot 10^{-9}$ $-1.16 \cdot 10^{-5}$	$1.21 \cdot 10^{-6}$ $-5.99 \cdot 10^{-4}$	$9.99 \cdot 10^{-8}$ $-4.15 \cdot 10^{-5}$	$2.30 \cdot 10^{-6}$ $1.14 \cdot 10^{-3}$
$[-130, -60]$	$-4.68 \cdot 10^{-6}$ $1.15 \cdot 10^{-7}$	$2.34 \cdot 10^{-10}$ $-6.95 \cdot 10^{-6}$	$-1.57 \cdot 10^{-8}$ $-5.43 \cdot 10^{-4}$	$-2.50 \cdot 10^{-8}$ $-5.73 \cdot 10^{-5}$	$1.04 \cdot 10^{-5}$ $9.38 \cdot 10^{-4}$
$[-250, -130]$	$-4.95 \cdot 10^{-7}$ $4.07 \cdot 10^{-8}$	$2.84 \cdot 10^{-11}$ $-1.44 \cdot 10^{-6}$	$-4.32 \cdot 10^{-8}$ $-2.01 \cdot 10^{-4}$	$-1.80 \cdot 10^{-9}$ $-6.54 \cdot 10^{-5}$	$-1.03 \cdot 10^{-5}$ $7.17 \cdot 10^{-4}$

Table A.4: Surface constants for the fitted surface at 420 m for anticlockwise moving protons.

y'	a_1 a_6	a_2 a_7	a_3 a_8	a_4 a_9	a_5 a_{10}
$[-60, -30]$	$-4.73 \cdot 10^{-6}$ $9.63 \cdot 10^{-7}$	$6.48 \cdot 10^{-9}$ $-2.47 \cdot 10^{-5}$	$-1.07 \cdot 10^{-6}$ $-7.41 \cdot 10^{-4}$	$-2.56 \cdot 10^{-7}$ $-6.95 \cdot 10^{-6}$	$-7.77 \cdot 10^{-5}$ $1.03 \cdot 10^{-3}$
$[-130, -60]$	$-1.10 \cdot 10^{-6}$ $4.11 \cdot 10^{-8}$	$-2.16 \cdot 10^{-10}$ $-1.59 \cdot 10{-5}$	$-8.54 \cdot 10^{-7}$ $-1.07 \cdot 10^{-3}$	$-6.99 \cdot 10^{-8}$ $-4.03 \cdot 10^{-5}$	$-1.10 \cdot 10^{-4}$ $1.58 \cdot 10{-3}$
$[-230, -130]$	$4.02 \cdot 10^{-7}$ $2.21 \cdot 10^{-8}$	$1.24 \cdot 10^{-11}$ $-3.06 \cdot 10^{-6}$	$-2.87 \cdot 10^{-8}$ $-4.52 \cdot 10^{-4}$	$-5.94 \cdot 10^{-8}$ $-5.27 \cdot 10^{-5}$	$-1.13 \cdot 10^{-5}$ $7.82 \cdot 10^{-4}$

Appendix B

Distributions of leading protons at 215 m and 308 m

The distribution of the leading protons measured at the 308 m and 338 m stations is shown in Fig. B.1. In the upper plot each colour corresponds to a ξ range $|\xi_{\mathrm{max}} - \xi_{\mathrm{min}}| = 10^{-3}$ and in the lower plot each colour corresponds to a θ_x^* range $|\theta_{x,\mathrm{max}}^* - \theta_{x,\mathrm{min}}^*| = 28$ μrad. The smallest ξ values lie on the top right corner of the distribution while the largest ξ values lie on the bottom left corner of the distribution. The same distribution in transformed coordinates is shown in Fig. B.2.

Figure B.3 displays the distribution of leading protons measured at 215 m and 225 m stations. In the upper plot each colour corresponds to a ξ range $|\xi_{\mathrm{max}} - \xi_{\mathrm{min}}| = 5 \cdot 10^{-3}$ and in the lower plot each colour corresponds to a θ_x^* range $|\theta_{x,\mathrm{max}}^* - \theta_{x,\mathrm{min}}^*| = 28$ μrad. Smallest ξ values are on the left of distribution. Figure B.4 shows the same distribution in transformed coordinates.

As can be seen in the aforementioned figures, different ξ values are well separated independently on θ_x^* and vice versa. In other words certain pair of measured observables correspond to a certain ξ value as well as a certain θ_x^* value. Thus ξ and θ_x^* can be reconstructed from two measured observables independently of each other.
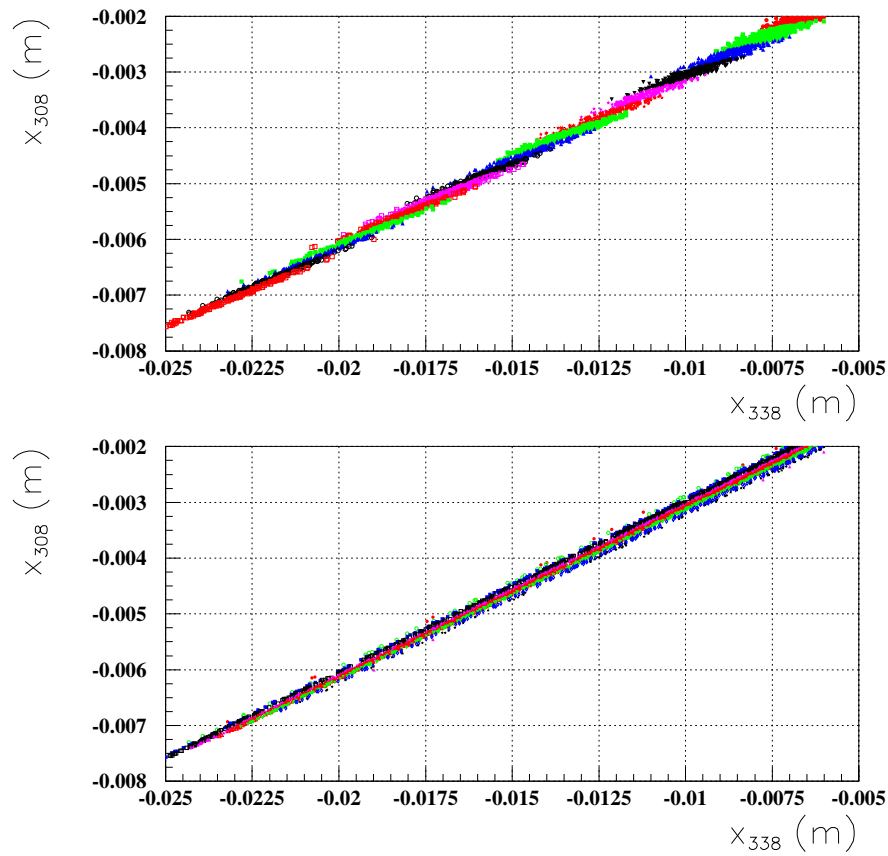
Figure B.1: Distribution of protons measured at the 308 m location. In the upper plot each colour corresponds to a ξ range of $|\xi_{\mathrm{max}} - \xi_{\mathrm{min}}|=10^{-3}$ while in the lower plot each colour corresponds to a θ_x^* range of $|\theta_{x,\mathrm{max}}^* - \theta_{x,\mathrm{min}}^*|=28$ μrad.
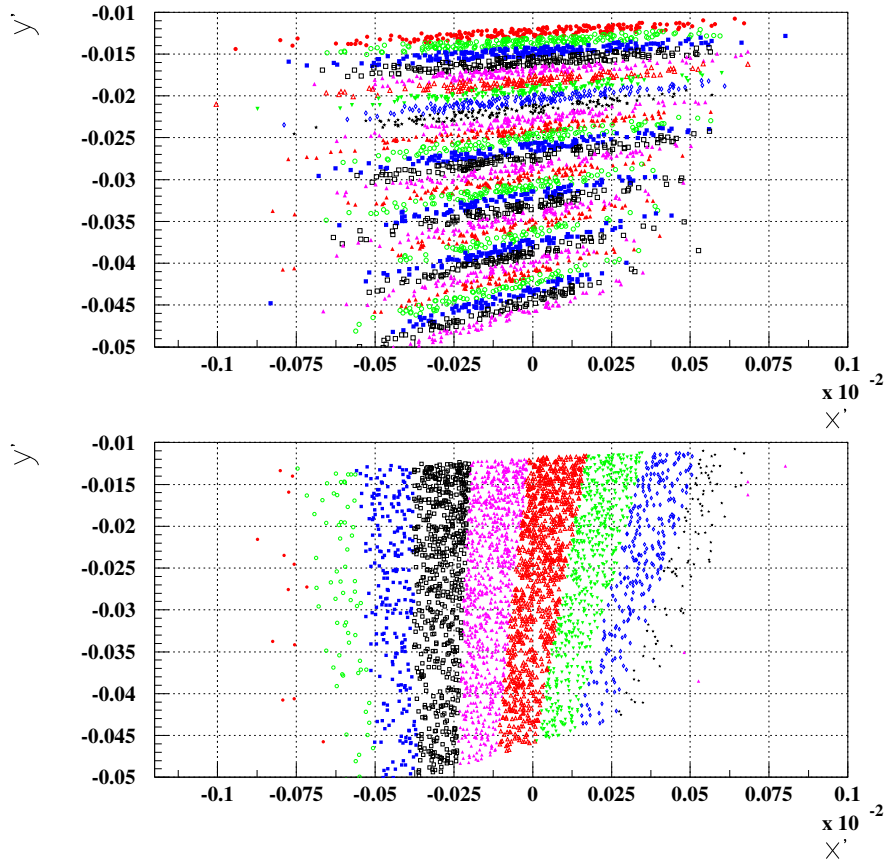
Figure B.2: Distribution of protons measured at the 308 m location after the coordinate transformation. In the upper plot each colour corresponds to a ξ range of $|\xi_{\max} - \xi_{\min}| = 5 \cdot 10^{-4}$ and in the lower plot each colour corresponds to a θ_x^* range of $|\theta_{x,\max}^* - \theta_{x,\min}^*| = 28$ μrad.